

**Spatial distribution of carbon and
oxygen isotopes in dolomite-cemented
layers and concretions of the Prairie
Canyon Member of the Mancos Shale,
western Colorado, USA**

Jeffrey S. Klein

This thesis is submitted in partial fulfillment of the degree of
Master of Science in Geochemistry

April, 1997

Department of Earth and Environmental Science
New Mexico Institute of Mining and Technology
Socorro, NM 87801

Abstract: Sandy, organic-rich mudrocks in the Prairie Canyon Member of the Mancos Shale host a number of stratabound dolomite-cemented concretions and laterally-extensive dolomite-cemented layers. Detailed, high-density sampling of five cemented horizons at three areal locations and four stratigraphic positions has permitted isotopic data to be analyzed within a three-dimensional framework, and at a variety of scales, ranging from mesoscopic (cm-m) to megascopic (> km). Taken together, all the cements (regardless of spatial position) show a remarkably linear correlation ($R^2 = 0.984$) between $\delta^{13}\text{C}$ and $\delta^{18}\text{O}$. Systematic center to edge decreases in both $\delta^{13}\text{C}$ and $\delta^{18}\text{O}$ exist in each of the cemented zones, and are persistent over lateral intervals of up to 1.5 km (and possibly more). In addition, each of the five horizons studied has a distinctive, laterally-persistent range of $\delta^{13}\text{C}$ and $\delta^{18}\text{O}$. These observations have important implications for geochemical correlation of low-permeability carbonate-cemented zones in the subsurface. The center to edge isotopic zonation suggests that dolomite precipitation began in the centers of the cemented zones, and then proceeded outward as isotopically lighter dolomite was added to the core zones during progressive burial. The $\delta^{13}\text{C}$ values offer strong evidence that the dolomite cements originated from CO_2 generated by decomposition of organic detritus. The centers of the cemented zones have positive $\delta^{13}\text{C}$ values (up to $> +10\text{‰}$, PDB) which resulted from incorporation of ^{13}C -enriched CO_2 that was produced as a by-product of methanogenesis. Conversely, the edges of the cemented zones have negative $\delta^{13}\text{C}$ values (down to $< -9\text{‰}$, PDB) which suggests incorporation of ^{13}C -depleted CO_2 from thermocatalytic decarboxylation reactions (i.e., at greater burial depths and higher temperatures). Oxygen isotope paleothermometry indicates that precipitation may have initiated at moderate temperatures (24-36°C) and ended at temperatures as high as 84°C.

TABLE OF CONTENTS

	Page
Abstract	
Table Of Contents	ii
Index of Tables	iv
Index of Figures	v
List of Abbreviations	vii
INTRODUCTION	1
REGIONAL GEOLOGY	2
SAMPLING STRATEGIES FOR GEOCHEMICAL ANALYSIS	7
METHODS	11
Sampling	11
Mineralogic composition determination	17
Stable isotopic analyses	17
Elemental composition determination	18
RESULTS	19
Mineralogic composition	19
Stable isotopic composition	24
<i>Cemented (grid) samples</i>	24
Sequence D (continuous layer)	36
Sequence A (continuous layer)	37
Sequence D (concretions)	38
Sequence C (concretion)	39
Sequence B (concretion)	40
<i>Host rock samples</i>	40
Elemental composition	42
DISCUSSION	49
$\delta^{18}\text{O}$ values in temperature-depth calculations	49
$\delta^{13}\text{C}$ as an indicator of organic diagenesis	51
Temporal relationship of isotopic data	54
Evaluation of alternative hypotheses	56
<i>Intrusion of meteoric water (mixing of two end-member fluids)</i>	57
<i>Precipitation of ^{18}O-enriched authigenic minerals</i>	58
<i>Late-stage recrystallization of early cement</i>	61
Comparison with data from other studies	63
Explanation of high minus-cement porosities	66
Spatial distribution of C and O isotopes	69
<i>Mesosopic (outcrop scale) isotopic zonation</i>	69
<i>Macro- and megascopic (regional scale) isotopic patterns: implications for geochemical correlation</i>	71

CONCLUSIONS	75
REFERENCES CITED	77
APPENDIX 1: Regional Structural Provinces	83
Uncompahgre Plateau	83
Douglas Creek Arch	84
Uinta and Piceance Creek Basins	85
References Cited (Appendix 1 only)	87
APPENDIX 2: CO₂ extraction for dolomite-calcite mixtures	89

INDEX OF TABLES

		Page(s)
Table 1	Previous Sampling Strategies	10
Table 2	Stable Isotope Results	14-15
Table 3	Point-Count Results	20-21
Table 4	Microprobe Results	44-45
Table 5	Summary of Isotopic Data by Layer	72

INDEX OF FIGURES

		Page
Figure 1	Field Area Location	3
Figure 2	Stratigraphic Setting	4
Figure 3	Grid 13 (photo)	12
Figure 4	Stratigraphic Correlation Diagram	13
Figure 5	Point-Count Results	23
Figure 6	Cement $\delta^{18}\text{O}$ - $\delta^{13}\text{C}$ Cross-Plot	25
Figure 7	Grid 9 Isotope Contours	26
Figure 8	Grid 11 Isotope Contours	27
Figure 9	Grid 13 Isotope Contours	28
Figure 10	Grid 15 Isotope Contours	29
Figure 11	Grid 16 Isotope Contours	30
Figure 12	Grid 18 Isotope Contours	31
Figure 13	Grid 10 Isotope Contours	32
Figure 14	Grid 12 Isotope Contours	33
Figure 15	Grid 14 Isotope Contours	34
Figure 16	Grid 17 Isotope Contours	35
Figure 17	Host Rock $\delta^{18}\text{O}$ - $\delta^{13}\text{C}$ Cross-Plot	41
Figure 18	Host Rock $\delta^{13}\text{C}$ Variation with Depth	43
Figure 19a,b	Microprobe Results (light vs. dark)	47
Figure 20	Microprobe Results (core vs. edge cement)	48

Figure 21	Depth-Stratified $\delta^{13}\text{C}$ Variation	52
Figure 22	Marine Dolomite Isotopic Data Compilation	64

LIST OF ABBREVIATIONS

BSE	back-scattered electron
c	core (isotopically heavy) sample
dol	dolomite
gac	grid sample above core
gbc	grid sample below core
hag	host rock above grid
hbg	host rock below grid
K-spar	potassium feldspar
MRF	metamorphic rock fragment
PCM	Prairie Canyon Member
PDB	PeeDee Belemnite
qtz	quartz
s	sample from vhrst
scc	septarian calcite
SMOW	Standard Mean Ocean Water
SRF	sedimentary rock fragment
tr	trace
vhrst	vertical host rock sampling traverse
VRF	volcanic rock fragment
XRD	X-ray Diffraction

INTRODUCTION

Diagenetic carbonate cements have received a considerable amount of attention in the literature for a variety of reasons. First, carbonate concretions often preserve an isotopic and chemical chronicle of the diagenetic evolution of the host sediments and their pore-waters. Therefore, models of concretion growth and internal zonation can be used to place geochemical data into a temporal framework (e.g., Gautier and Claypool, 1984; Scotchman, 1991; Mozley and Carothers, 1992; and others). Second, carbonate cements are of interest to the petroleum community because of their potential to reduce primary permeability and affect fluid migration. Although isolated concretions only affect fluid flow locally, coalesced concretions can form laterally continuous cemented horizons (Bjørkum and Walderhaug, 1990) that can retard, or even eliminate, vertical fluid flow. In extreme circumstances, this can lead to compartmentalization of the reservoir and associated production problems (Kantorowicz et al., 1987). Thus, understanding the geometry and spatial distribution of carbonate cements is fundamental to effective reservoir exploitation.

The purpose of this study is to present spatially distributed geochemical and petrographic data from the dolomite-cemented concretions and laterally continuous horizons of the Upper Cretaceous Prairie Canyon Member (PCM) of the Mancos Shale. Comprehensive, high-density sampling of cemented zones that are traceable in outcrop over intervals of several kilometers has revealed a remarkably uniform isotopic distribution, both at local and regional scales.

Because local, small-scale isotopic zonation appears to be persistent over large lateral intervals (at least 1.5 km), the possibility exists for subsurface correlation of the Prairie Canyon cements. The geochemical data also provides information about the mode of growth of laterally-extensive cemented layers and concretions in organic-rich mudrocks.

REGIONAL GEOLOGY

The field area for this study is situated at the type locality of the Prairie Canyon Member of the Mancos Shale. The type area is located 23 miles northwest of Grand Junction, in Mesa County, Colorado (Fig. 1). The Prairie Canyon type area is bounded by four major physiographic provinces: the Uncompahgre Plateau to the south; the Douglas Creek Arch to the north; and the Uinta and Piceance Creek Basins to the west and east, respectively.

Stratigraphically, the Prairie Canyon Member (formerly known as the 'Mancos B' interval; Kopper, 1962) sits between the Upper and Lower Blue Gate Members of the Mancos Shale. The PCM is 1,005 feet (306 m) thick and has been subdivided into three informal intervals at the type locality: lower, middle and upper (Fig. 2). The lower interval is 360 feet (110 m) thick, and the upper interval is 413 feet (126 m) thick. The middle interval, which is the focus of this investigation, is 233 feet (71 m) thick (Cole et al., submitted).

Figure 1: Field area location. Adapted from Cole and Young (1991).

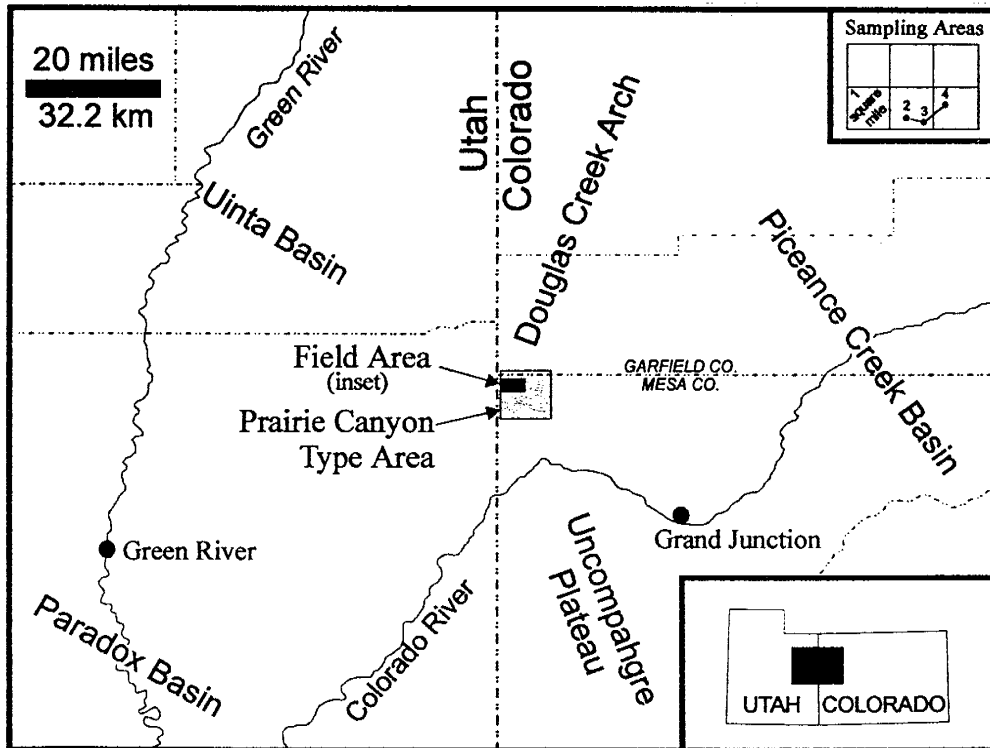
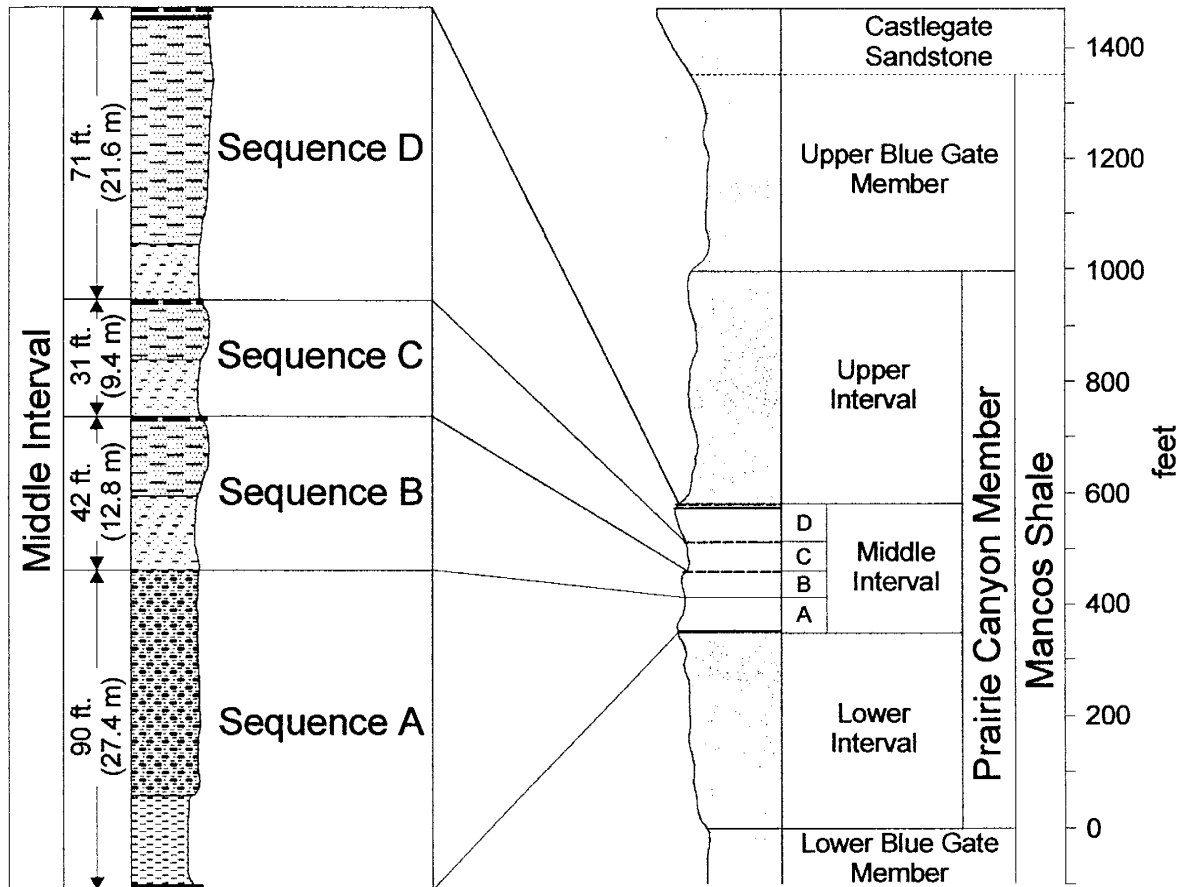


Figure 2: Stratigraphic setting and lithologies of the middle interval of the Prairie Canyon Member of the Mancos Shale. Adapted from Cole and Young (1991).



The Mancos Shale was deposited atop the Dakota Sandstone at the floor of the Western Interior Seaway during Upper Cretaceous time (Cole and Young, 1991). Ranging in thickness from 1,067 m to 1,524 m (Young, 1955, 1959; Kopper, 1962), the Mancos consists of gray to black calcareous shale with zones of sandy shale and carbonate concretions. It is capped by the more resistant Mesaverde Group in the upper part of the Book Cliffs of western Colorado and eastern Utah (Young, 1960).

The Mancos Shale has traditionally been subdivided into three members: Tununk, Juana Lopez (Ferron), and Blue Gate. Recently, however, Cole et al. (submitted) have officially named an additional unit, the Prairie Canyon Member. The PCM is situated in the upper third of the Mancos Shale and splits the Blue Gate Shale into upper and lower submembers (Fig. 2). The PCM is more sandy than the lower part of the Mancos and contains commercial quantities of natural gas.

The upper and lower contacts of the Prairie Canyon Member are defined in the subsurface by abrupt geophysical log kicks. The basal contact with the Lower Blue Gate Shale Member occurs at approximately 2,300 feet (701 m) above the top of the Dakota Sandstone. It is marked by a sudden upward change from silty claystone to interlaminated sandstone and shale, and a corresponding shift from high to low gamma-ray values. An opposite shift in gamma-ray values marks the upper contact of the PCM at 300-500 feet (91-152 m) below the top of the Castlegate Sandstone, which extends into the Mancos from the west. Two tongues of the Mancos Shale (Buck Tongue and Anchor

Mine Tongue) are present above the Castlegate Sandstone in the Prairie Canyon area (Cole et al., submitted).

The Prairie Canyon Member has been identified in wells throughout the Douglas Creek Arch area. It is present in the subsurface throughout the southern part of the Uinta Basin to the west where it grades into the much thicker and sandier Emery Sandstone (Fouch and Cashion, 1979). To the east, the PCM extends at least as far as the Piceance Creek Dome (Kellogg, 1977). At the surface, the Prairie Canyon Member forms a broad, poorly defined outcrop belt near the base of the Book Cliffs from Grand Junction, Colorado to near Woodside, Utah.

Cole & Young (1991) and Cole et al. (submitted) have provided detailed stratigraphic, paleogeographic, and sedimentological descriptions of the Prairie Canyon Member, and their work is the basis for the remainder of this section. The middle interval consists of four well-defined coarsening-upward parasequences that are separated by transgressive marine flooding surfaces. These parasequences are informally referred to as sequences A, B, C, and D (Fig. 2). Sequence A grades from silty claystone to a sandstone-claystone composite and features a thin (~30 cm) continuously-cemented sandy dolomite layer at its base. Sequences B, C, and D are each made up of sandy siltstone that coarsens upward into bioturbated muddy sandstone. Stratabound concretions of sandy ferroan dolomite cap each of the three upper parasequences. In addition, a laterally continuous cemented layer occurs just below the concretions at the top of Sequence D.

The Prairie Canyon sediments may have originated from several late Santonian and early Campanian wave-dominated deltaic systems (e.g., Emery, Star Point, and Blackhawk) located along the western shore of the Western Interior Seaway. Fine-grained sediments from these sources may have migrated offshore in prodelta plumes via storm-generated, shore-parallel, downwelling currents to be deposited below storm wave base. Southeast-trending (111°) paleocurrent vectors in the Prairie Canyon type area suggest that the sediments were derived from the northwest. The coarsening-upward sequences (A-D) that comprise the middle interval of the PCM may represent regressive prodelta deposits. At the top of each regressive sequence, a sea level rise may have cut off the sediment supply to the more distal (deeper) offshore areas and allowed carbonate precipitation and pelagic sedimentation.

SAMPLING STRATEGIES FOR GEOCHEMICAL ANALYSIS

A variety of sampling strategies have been employed in geochemical studies of carbonate cements, and many studies have shown that geochemical heterogeneity can exist at a variety of scales. Reservoir geologists and engineers recognize four different levels of scale: (1) microscopic (i.e., $\mu\text{m-cm}$); (2) mesoscopic (cm-m); (3) macroscopic (m-km); and (4) megascopic ($> \text{km}$; Alpay, 1972). Many geochemical studies of carbonate cements (see below) have examined *either* small-scale (micro- to mesoscopic) *or* large-scale (macro- to megascopic) geochemical variation in *either* a regional (lateral) *or*

stratigraphic (vertical) context. However, few studies have attempted to analyze geochemical data at multiple scales and in both contexts. Previous methods of sample collection for geochemical analysis include the following:

- (1) Obtaining single “grab” samples from individual concretions (e.g., Sass and Kolodny, 1972; *Note*: these workers also did center-to-edge sampling; see # 3 below).
- (2) Collecting samples from outcrops or drill core over macroscopic vertical intervals (e.g., Pisciotto and Mahoney, 1981; Morad et al., 1990).
- (3) Mesoscopic sampling of concretions or cemented layers from center-to-edge or edge-to-center-to-edge along vertical traverses (e.g., Sass and Kolodny, 1972; Irwin, 1980; Walderhaug et al., 1989; Wilkinson, 1991, 1992).
- (4) Combined horizontal and vertical mesoscopic sampling traverses (e.g., Wilkinson, 1993; Scotchman, 1991, Raiswell, 1976).
- (5) Semi-random two dimensional mesoscopic sampling of cross-sections of concretions (e.g., Hennessy and Knauth, 1985).
- (6) Mesoscopic sampling of vertical cross-sections of cemented layers in a two dimensional grid pattern (10 cm grid spacing; e.g., Bjørkum and Walderhaug, 1993).
- (7) Nesting of mesoscopic vertical sampling traverse data sets (type 3 above) within a regional (megascopic) and stratigraphic framework (Walderhaug et al., 1989).

The advantages and limitations of each of these sampling strategies are summarized in Table 1.

Detailed mesoscopic sampling of cemented zones (i.e., types (3)-(6); Table 1) has drawn attention to the fact that considerable carbon and oxygen isotopic variation may exist across intervals of only a few centimeters. In certain cases, the variation may occur as zonation that is a distinguishing characteristic of the cemented zone at a given locality. If the same, or similar, isotopic zonation exists at multiple sampling localities, the possibility exists for regional geochemical correlation of cemented zones. This would require that mesoscopic data sets be nested within the larger regional (megascopic) and stratigraphic framework (i.e., type (7); Table 1).

The more samples that are collected at a given locality, the higher the likelihood of resolving local isotopic zonation. A single sample collected from a given locality (i.e., types (1) and (2); Table 1) cannot provide a representative cross-section of the local mesoscopic isotopic distribution. Similarly, centimeter-scale vertical sampling traverses (i.e., type (3); Table 1) may or may not expose a local isotopic zonation because of their one-dimensional (e.g., only vertical) nature. Therefore, mesoscopic sampling should be extended in the horizontal direction as well as the vertical direction (i.e., types (4)-(6); Table 1) whenever possible. The most detailed example of bidimensional mesoscopic sampling to date is the gridding method (i.e., type (6); Table 1) of Bjørkum and Walderhaug (1993).

Table 1: Overview of previous sampling strategies for geochemical analysis of carbonate cements.

<i>method</i>	<i>scale</i>	<i>advantages</i>	<i>limitations</i>	<i>reference(s)</i>
(1) one sample per concretion	N/A	none	cannot resolve local mesoscopic isotopic zonations	Sass and Kolodny, 1972
(2) large-scale vertical sampling through a stratigraphic section	tens to hundreds of meters (macroscopic)	allows comparison of geochemical data within a stratigraphic framework	unidimensional: cannot resolve mesoscopic isotopic zonations at individual sampling localities	Pisciotta and Mahoney, 1981; Morad et al., 1990
(3) small-scale vertical sampling	cm to tens of cm (mesoscopic)	shows vertical component of isotopic spatial distribution	unidimensional: no horizontal spatial component of mesoscopic isotopic distribution	Irwin, 1980; Walderhaug et al., 1989; Sass and Kolodny, 1972; Wilkinson, 1991, 1992
(4) small-scale vertical and horizontal sampling	cm to tens of cm (mesoscopic)	bidimensional: can show isotopic variation in both horizontal and vertical directions	data cannot be contoured well with only a single horiz. and vert. transect	Wilkinson, 1993; Scotchman, 1991; Raiswell, 1976
(5) small-scale semi-random sampling within concretions	cm to tens of cm (mesoscopic)	bidimensional: isotopic data can be contoured on a scaled diagram of the outcrop	more difficult to contour than simple grids; cannot make inferences about 3-D spatial distribution of C and O isotopes	Hennessy and Knauth, 1985
(6) sampling in a grid pattern	cm to tens of cm (mesoscopic)	bidimensional: can show complete spatial distribution of C and O isotopes in 2 dimensions by contouring data on scaled diagrams of outcrops; easier to contour than (5)	cannot make inferences about 3-D spatial distribution of C and O isotopes; sampling intensive	Bjørkum and Walderhaug, 1993
(7) nesting of mesoscopic data sets within a regional (megascopic) and stratigraphic framework	local (mesoscopic) sampling separated by hundreds to thousands of meters (macro- to megascopic)	allows for comparison of geochemical data at multiple levels of scale	mesoscopic data limited if only sampled in vertical traverses (i.e., same as (3) above). This could be avoided by using (4), (5), or (6) to characterize local isotopic distribution.	Walderhaug et al., 1989

METHODS

Sampling

We used high-density, mesoscopic sampling to geochemically characterize individual cemented outcrops within the middle interval of the Prairie Canyon Member. The outcrop scale (mesoscopic) data sets were then analyzed within the stratigraphic framework provided by Cole and Young (1991). This method allowed the comparison of small-scale geochemical data sets between outcrops of the same cemented layer over lateral intervals of up to 1.5 kilometers.

The gridding method of Bjørkum and Walderhaug (1993; type (6) of Table 1) was used to characterize local mesoscopic isotopic zonation. Ten vertical, two-dimensional grids were established perpendicular to bedding (as in Fig. 3) on cemented outcrops at three locations (Areas 2, 3, and 4; Fig. 4). A battery-powered hand drill equipped with a ¼ inch masonry bit was used to obtain powdered samples at the intersection of grid lines. Typical grid spacing was 10cm x 10cm, but the grid spacing varied between 5 cm and 30 cm. A 5cm x 5cm subgrid was collected in Grid 11 (main grid spacing 10cm x 10cm) as a further check of scale. In addition, three consecutive samples were removed at different drilling depths from hole Z2 (samples Z2-A, B, and C; Table 2) of Grid 11 to check for isotopic variation outside the vertical plane of the grid. Between 16 and 48 samples were collected per grid.

Figure 3: Samples were collected in vertical grids such as Grid 13 (pictured).



Figure 4: Lateral and stratigraphic position of sampling localities (adapted from Cole and Young, 1991).

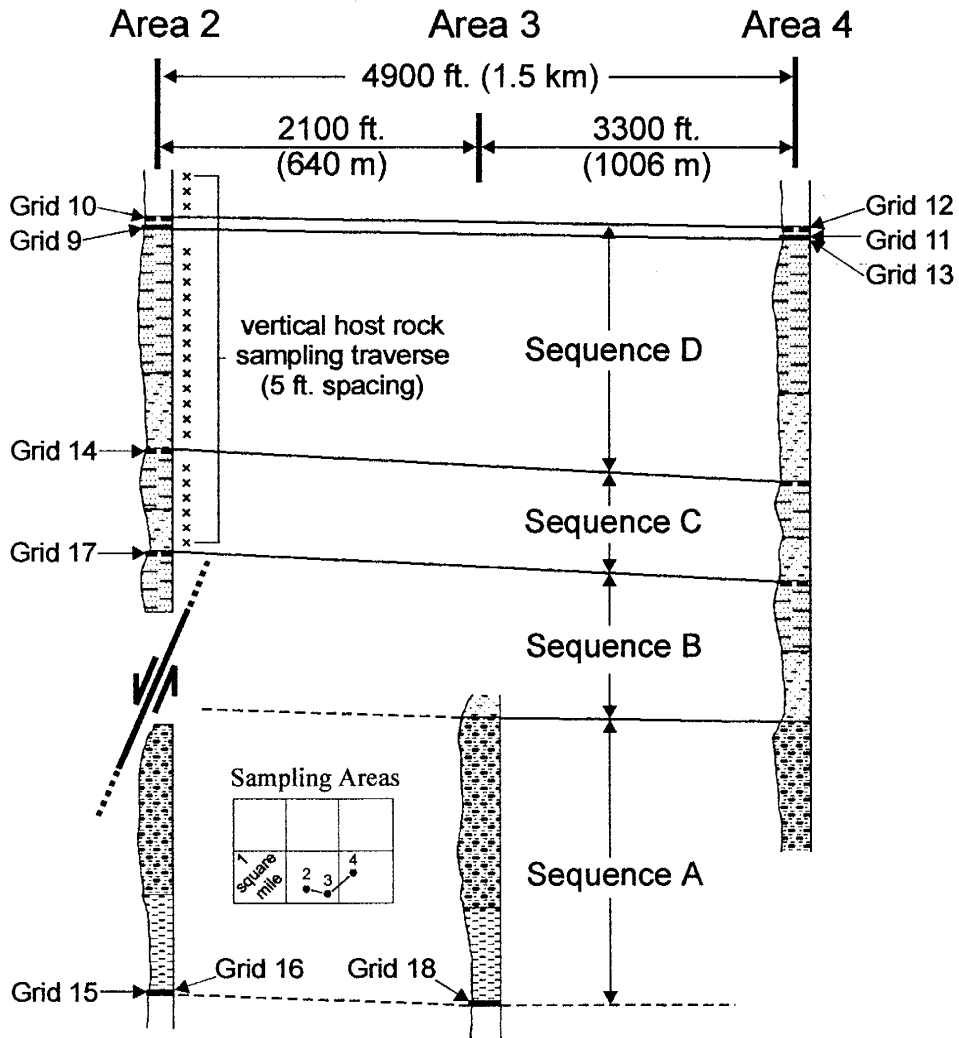


Table 2: Results of 324 stable isotopic analyses. Abbreviations: 'hag' = host above grid; 'hbg' = host below grid; 's' = sample from vertical host rock sampling traverse; 'scc' = septarian calcite.

sample	$\delta^{13}\text{C}$ PDB	$\delta^{18}\text{O}$ SMOW	sample	$\delta^{13}\text{C}$ PDB	$\delta^{18}\text{O}$ SMOW	sample	$\delta^{13}\text{C}$ PDB	$\delta^{18}\text{O}$ SMOW	sample	$\delta^{13}\text{C}$ PDB	$\delta^{18}\text{O}$ SMOW
Grid 9			f2	-0.73	24.34	z1	-5.85	21.85	d5	3.29	26.51
z1	-6.28	22.03	a3	7.71	28.73	a1	-6.19	21.93	e5	2.45	26.42
a1	-8.38	21.41	b3	7.76	28.71	b1	-6.14	22.15	b6	1.59	25.30
b1	-8.74	21.32	c3	6.67	28.41	c1	-6.10	21.86	b'2	-2.51	23.82
c1	-9.20	21.18	d3	5.52	27.63	d1	-5.80	22.15	b2.5	2.48	26.33
d1	-9.70	20.73	e3	3.97	26.91	e1	-6.14	21.90	b'2.5	2.29	26.12
e1	-7.47	20.81	f3	3.51	26.71	x2	-1.21	24.18	c2.5	2.48	26.35
z2	-0.71	24.91	a4	10.74	30.39	y2	-1.59	23.98	b'3	3.95	27.10
a2	-3.05	23.23	b4	8.31	28.71	z2-A	-0.71	24.45	Grid 12		
b2	-1.97	23.98	c4	8.28	29.06	z2-B	-0.56	24.62	a1	4.20	27.07
c2	-1.92	24.00	d4	7.03	28.91	z2-C	-0.60	24.83	a2	6.56	28.39
d2	-4.15	23.05	e4	5.82	28.17	a2	-0.73	24.75	a3	8.29	29.48
e2	-5.63	22.16	f4	4.95	27.70	b2	-2.04	23.90	a4	8.48	29.38
z3	4.37	27.46	a5	10.07	30.21	c2	-2.55	23.74	a5	10.73	30.36
a3	3.10	26.90	b5	10.71	30.34	d2	-2.47	23.60	a6	9.35	29.53
b3	3.43	27.09	c5	8.40	29.24	e2	-2.29	23.67	a7	10.09	30.33
c3	4.31	27.14	d5	7.21	29.08	x3	3.69	26.95	a8	10.35	30.24
d3	3.06	26.72	e5	4.80	27.63	y3	3.71	26.92	a9	8.61	29.47
e3	-0.82	24.57	f5	4.82	27.53	z3	4.82	27.48	a10	8.02	29.35
z4	7.19	28.98	a6	9.41	29.63	a3	4.28	27.18	a11	7.07	28.93
a4	4.94	27.74	b6	10.41	30.22	b3	4.13	27.06	a12	5.19	27.75
b4	5.81	28.28	c6	7.74	28.89	c3	4.25	27.22	b2	6.09	28.29
c4	6.25	28.41	d6	5.83	28.01	d3	3.94	26.91	b5	10.01	30.12
d4	6.03	28.32	e6	2.93	26.59	e3	3.58	26.89	b8	9.11	29.60
e4	3.10	26.90	f6	3.12	26.70	f3	3.25	26.80	b11	6.76	28.59
a5	0.70	24.96	a7	7.13	28.77	x4	6.75	28.65	c2	5.17	27.51
b5	1.77	25.71	b7	7.99	29.25	y4	6.93	28.86	c5	9.55	29.91
c5	2.41	26.13	c7	6.46	28.46	z4	7.30	28.84	c8	4.98	27.75
d5	-1.44	24.08	d7	3.11	26.86	a4	6.99	29.14	c11	5.40	28.17
e5	-0.65	24.65	e7	-0.70	24.63	b4	6.08	28.10	d5	7.68	29.28
Grid 10			f7	-2.45	23.86	c4	6.64	28.70	d8	6.23	28.48
a1	1.57	25.73	a8	4.27	27.12	d4	5.94	28.07	d11	-0.76	24.50
b1	2.57	26.35	b8	6.04	28.17	e4	5.81	28.12	e5	6.81	28.80
c1	2.94	26.77	c8	4.42	27.20	f4	5.78	28.01	e8	5.11	27.94
d1	2.94	26.62	d8	-0.61	24.48	x5	5.22	27.78	f5	7.07	28.75
a2	6.31	28.04	e8	-4.88	22.58	y5	5.16	27.75	f8	6.60	28.61
b2	5.34	27.76	scc	-2.56	16.99	z5	5.24	27.50	g8	1.72	25.96
c2	5.11	27.66	Grid 11			a5	4.74	27.51	scc	-3.47	15.19
d2	4.68	27.49	x1	-5.86	22.02	b5	3.48	26.56	1	2.53	17.47
e2	2.42	26.29	y1	-5.09	22.36	c5	3.87	26.87	2	9.75	21.07
									3	0.03	17.51

Table 2: Stable isotope results (cont.).

sample	$\delta^{13}\text{C}$ PDB	$\delta^{18}\text{O}$ SMOW	sample	$\delta^{13}\text{C}$ PDB	$\delta^{18}\text{O}$ SMOW	sample	$\delta^{13}\text{C}$ PDB	$\delta^{18}\text{O}$ SMOW	sample	$\delta^{13}\text{C}$ PDB	$\delta^{18}\text{O}$ SMOW
Grid 13			h5	6.57	28.38	a2	1.60	25.44	b3	5.46	27.80
a6	1.79	25.59	h4	5.29	27.65	a3	5.23	27.76	b4	5.07	27.75
a5	4.76	27.44	h3	2.66	26.28	a4	5.67	28.09	b5	2.26	26.28
a4	4.78	27.79	h2	-5.41	22.11	a5	3.71	27.09	c1	1.48	24.96
a3	1.14	25.24	h1	-8.77	21.03	a6	-0.25	24.56	c2	3.30	26.08
a2	-4.86	22.54	Grid 14			b1	-3.18	23.34	c3	5.47	27.70
a1	-6.87	22.33	a3	-4.07	22.52	b2	1.62	25.61	c4	4.74	27.45
b6	1.49	25.53	b2	-4.05	22.58	b3	5.21	27.78	c5	0.93	24.91
b5	5.69	28.02	b3	-3.99	22.50	b4	5.57	28.11	Host Rock		
b4	4.81	27.57	b4	-4.44	21.99	b5	4.62	27.55	s0	0.49	24.87
b3	1.36	25.21	c1	-4.55	22.36	b6	0.94	25.61	s1	0.44	24.62
b2	-3.99	22.73	c2	-3.85	22.82	c1	-3.76	22.87	s2	0.35	24.58
c6	1.47	25.33	c3	-3.90	22.67	c2	0.26	24.32	s3	0.32	24.37
c5	5.25	27.78	c4	-4.76	22.32	c3	3.50	26.78	s4	0.32	24.17
c4	6.86	28.79	d1	-4.30	22.52	c4	5.62	27.97	s5	0.29	27.12
c3	3.25	26.94	d2	-3.66	22.95	c5	4.58	27.57	s6	0.38	24.77
c2	-3.09	23.34	d3	-3.58	22.87	c6	1.09	25.32	s7	0.34	24.20
c1	-8.28	21.31	d4	-4.13	22.80	Grid 17			s8	0.60	24.65
d6	1.65	25.32	e2	-4.21	22.67	a2	-8.85	20.95	s9	0.61	24.60
d5	5.47	27.81	e3	-3.71	22.76	a3	-6.12	21.59	s10	0.44	24.17
d4	6.63	28.60	e4	-4.54	22.30	a4	-8.16	21.13	s11	0.27	23.99
d3	3.32	26.84	f3	-4.00	22.65	b1.4	-7.32	21.00	s12	0.43	24.31
d2	-3.06	23.27	Grid 15			b2	-5.96	21.50	s13	0.49	23.93
d1	-8.24	21.34	a0	-4.05	23.39	b3	-4.49	22.12	s14	0.43	23.99
e6	1.84	25.45	b0	-3.44	23.06	b4	-4.49	22.23	s15	0.61	24.32
e5	6.09	28.08	c0	-1.70	23.68	c1	-5.82	21.92	s16	-3.62	21.24
e4	6.98	28.68	a1	-0.52	24.43	c2	-4.85	22.20	s17	1.25	24.66
e3	3.32	26.61	a2	2.74	26.44	c3	-4.24	22.52	s18	8.41	29.33
e2	-2.97	23.25	a3	5.42	27.83	c4	-4.66	22.45	s20	-0.39	23.20
e1	-7.68	21.39	a4	5.29	27.98	d1	-6.01	21.63	s21	0.72	25.29
f6	1.56	25.44	a5	2.42	26.46	d2	-5.00	22.32	s22	0.60	24.83
f5	5.60	27.78	b1	-0.24	24.15	d3	-4.08	22.53	s23	0.64	25.16
f4	6.96	28.74	b2	2.97	26.27	d4	-4.31	22.48	hag9	-5.61	21.02
f3	3.44	27.02	b3	5.44	27.79	e2	-4.93	22.30	hbg10	0.79	25.12
f2	-3.13	23.22	b4	5.10	27.70	e3	-4.05	22.48	hag11	-10.26	20.49
f1	-7.91	21.26	b5	2.11	26.26	Grid 18			hbg11	0.67	24.88
g6	0.36	24.59	c1	0.60	24.52	a1	3.48	23.92	hbg11	0.75	24.84
g5	5.67	27.87	c2	3.15	26.30	a2	2.74	26.35	hbg12	0.73	26.83
g4	6.67	28.49	c3	5.48	27.82	a3	5.31	27.76	hbg13	0.62	24.62
g3	3.33	26.98	c4	4.69	27.47	a4	4.85	27.62	hag14	-4.61	21.43
g2	-3.62	22.96	c5	1.40	25.37	a5	3.24	26.63	hbg14	-1.47	22.54
g1	-8.15	21.25	Grid 16			b0	-3.23	22.69	hbg14	-1.35	21.68
h6	2.17	25.62	a1	-2.79	23.21	b1	1.18	24.81	hbg15	0.28	24.94
						b2	3.52	26.40	hbg18	0.35	24.77

Figure 4 illustrates the sampling strategy in its stratigraphic and areal context. We sampled two laterally continuous cemented layers (one at the bottom of Sequence A and another just below the top of Sequence D) and three concretionary horizons (at the tops of Sequences B, C, and D) within the Prairie Canyon Member. Three grids were collected from the continuous layer of Sequence D (Grid 9 at Area 2 and Grids 11 and 13 at Area 4). Similarly, three grids were collected from the continuously cemented layer at the base of Sequence A (Grids 15 and 16 at Area 2 and Grid 18 at Area 3). Two grids (Grid 10 at Area 2 and Grid 12 at Area 4) were sampled from concretions at the top of Sequence D. Grids 17 and 14 (Area 2) were established on isolated concretions marking the tops of Sequences B and C, respectively. Hand samples were quarried from each of the grids for petrographic analysis.

In addition to the grid samples, a number of samples were collected from the host rock for thin sections and isotopic analyses. Host rock samples were collected from several centimeters above and below each grid. In addition, a vertical sampling traverse was made from the base of Sequence C to just above the top of Sequence D. Host rock samples were collected at five foot intervals along the traverse (Fig. 4).

Mineralogic composition determination

Mineralogic composition was characterized by X-ray diffraction (XRD) and by petrographic examination. The XRD data were collected at the New Mexico Bureau of Mines and Mineral Resources' X-ray laboratory using a Rigaku D/MAX-II diffractometer driven by MDI's JADE/Datascan software package. Quantitative mineral abundances were determined by 300-point point-counts of 24 thin sections (stained for K-spar and calcite). Visual estimates under cathodoluminescence (using a MAAS/Nuclide ELM-3 luminoscope) were used as a check of the relative abundances of quartz and feldspar. Mineral abundances were rounded to the nearest percent, and abundances less than 0.5% are reported as trace (tr).

Stable isotopic analyses

Carbon and oxygen isotopic compositions were determined for 324 cemented and host rock samples at the New Mexico Tech Stable Isotope Laboratory. Powdered grid samples that had been extracted with the hand drill did not need to be crushed, but host rock hand samples were crushed and sieved through a 100-mesh screen. Forty milligram aliquots of the powdered samples were then reacted under vacuum with 100% phosphoric acid in a 50°C water bath for 12 hours. This method is a variation of the technique described by Rosenbaum and Sheppard (1986; itself a variation of the method of McCrea, 1950). The resulting CO₂ gas was extracted on a carbonate vacuum extraction

line and analyzed on a Finnigan MAT Delta E isotope ratio mass spectrometer using OzTech gas standards.

Thirty-four host rock samples were determined to have a mixture of calcite and dolomite. These samples were allowed to react with 100% phosphoric acid at 25°C on the carbonate extraction line with the reaction vessels open to the pump for 90 minutes (see Appendix 2). This allowed calcite, which reacts readily at room temperature, to be consumed and separated from the slow-reacting dolomite. This 'open-vessel' extraction technique is described in Phillips et al. (1992). Afterwards, the remainder of the sample (dolomite) was placed in a 50°C water bath and analyzed as above.

The oxygen isotope data was corrected for phosphoric acid fractionation using the acid fractionation relationship of Rosenbaum and Sheppard (1986) for dolomite:

$$10^3 \ln \alpha_{\text{CO}_2(\text{g})-\text{CaMg}(\text{CO}_3)_2} = 6.65 \times (10^5/T^2) + 4.23$$

This relationship yields a $\Delta_{\text{CO}_2(\text{g})-\text{CaMg}(\text{CO}_3)_2}$ value of 10.60‰ at 50°C.

Elemental composition determination

Elemental composition of the carbonate cement was determined by electron microprobe analyses. The analyses were performed at the University of New Mexico Department of Earth and Planetary Science on a recently upgraded JEOL-733 Superprobe. The system is equipped with a high-resolution back-scattered electron (BSE) detector, X-ray mapping features, and image analysis software. Dolomite, calcite, siderite, spessartine, and celestite mineral

standards were used to standardize the microprobe for Mg, Ca, Fe, Mn, and Sr, respectively. Analytical precision is estimated to be within 2% of the reported values. Compositional variation within the dolomite cement was identified with BSE imaging and quantified with spot microprobe analyses.

RESULTS

Mineralogic composition

X-ray diffraction analyses indicate that dolomite is the dominant carbonate phase present in the cemented layers (grid samples). However, host rock samples contain both dolomite and calcite. Quartz is present in both types of samples. The XRD data are confirmed by the results of point-counts of 24 thin sections (Table 3).

Of the 24 thin sections, 18 are from cemented zones (continuous layers or stratabound concretions). Dolomite cement accounts for between 50 and 85 percent of the volume of these layers. The framework grains in the cemented zones are 5 to 28 percent quartz, trace to 4 percent feldspar, and 0 to 6 percent lithic fragments (mainly chert). Opaque framework grains comprise an additional 1 to 11 percent. Taken together, clays and opaque matrix minerals account for 3 to 9 percent of the cemented zones. In general, there is no porosity in the cemented samples.

The remaining six thin sections are from the vertical host rock sampling traverse and from host rock above or below grids. Although present in smaller

Table 3: Point-count results.

Grid Samples						
grid	9	10	10	10	11	11
sample	B'5	B7	B'5	B1	A2	A3
type	gbc	gbc	c	gac	gac	gac
quartz	27.8	10.0	14.0	15.0	18.8	12.3
feldspar	4.0	1.0	1.5	2.2	2.3	1.5
VRF	0.0	0.0	0.0	0.6	0.0	0.0
SRF	5.5	4.5	0.0	0.6	0.0	0.0
MRF	0.0	0.0	0.0	0.0	0.0	0.3
porosity	0.0	0.0	0.0	0.0	0.0	0.0
authigenic dol	49.3	73.5	74.0	66.0	69.0	76.6
detrital calcite	0.0	0.0	0.0	0.0	0.0	0.0
undiff. clays	1.4	0.0	1.0	0.6	5.3	1.0
opaque grains	7.8	5.5	3.8	10.5	1.4	5.0
opaque matrix	4.2	5.5	4.8	4.5	3.2	3.3
opaque cement	0.0	0.0	0.9	0.0	0.0	0.0
total	100.0	100.0	100.0	100.0	100.0	100.0
grains	45.1	21.0	19.3	28.9	22.5	19.1
cement	49.3	73.5	74.9	66.0	69.0	76.6
matrix	5.6	5.5	5.8	5.1	8.5	4.3
total	100.0	100.0	100.0	100.0	100.0	100.0

Grid Samples (cont.)						
grid	11	11	11	12	12	12
sample	A4	A5	E3	A4	B8	A6
type	c	gbc	gac	c	gbc	c
quartz	9.3	14.6	16.1	11.6	9.5	4.5
feldspar	1.1	0.5	0.7	1.2	1.0	0.5
VRF	0.0	0.0	0.0	0.0	0.0	0.0
SRF	0.0	0.0	6.1	2.3	3.0	1.0
MRF	0.0	0.0	0.0	0.0	0.0	0.0
porosity	0.0	2.0	0.0	0.3	0.0	0.0
authigenic dol	79.3	70.6	69.1	76.0	79.5	85.5
detrital calcite	0.3	1.0	0.0	0.0	0.0	0.0
undiff. clays	2.0	0.3	0.0	0.0	0.5	0.0
opaque grains	3.2	5.5	3.2	2.6	2.4	3.4
opaque matrix	4.8	5.5	4.8	6.0	2.8	5.1
opaque cement	0.0	0.0	0.0	0.0	1.3	0.0
total	100.0	100.0	100.0	100.0	100.0	100.0
grains	13.9	22.0	26.1	17.8	15.9	9.4
cement	79.3	72.0	69.1	76.2	80.8	85.5
matrix	6.8	5.9	4.8	6.0	3.3	5.1
total	100.0	100.0	100.0	100.0	100.0	100.0

Table 3: Point count results (cont.).

Grid Samples (cont.)						
grid	12	13	13	17	18	18
sample	B11(3)	A2	A3	D4	A1	A4
type	gbc	gac	gac	c	gac	c
quartz	11.0	23.0	20.6	13.3	7.0	6.0
feldspar	1.5	1.5	0.4	0.8	1.4	0.4
VRF	0.0	0.0	0.0	0.0	0.0	0.3
SRF	5.5	5.0	2.0	0.0	0.0	0.0
MRF	0.0	0.0	0.0	0.0	0.0	0.0
porosity	0.0	3.0	1.0	0.0	0.0	0.0
authigenic dol	69.0	55.6	64.0	69.3	75.3	84.3
detrital calcite	0.0	0.0	0.0	1.0	2.0	0.0
undiff. clays	1.0	2.3	0.0	0.0	0.0	0.0
opaque grains	7.2	6.7	7.2	10.9	8.6	4.5
opaque matrix	4.8	2.9	4.8	4.7	5.7	4.5
opaque cement	0.0	0.0	0.0	0.0	0.0	0.0
total	100.0	100.0	100.0	100.0	100.0	100.0
grains	25.2	37.3	30.5	26.0	19.0	11.2
cement	69.0	57.3	64.6	69.3	75.3	84.3
matrix	5.8	5.4	4.8	4.7	5.7	4.5
total	100.0	100.0	100.0	100.0	100.0	100.0

Host Rock Samples						
grid	vhrst	vhrst	9	11	11	14
sample	S0	S6	above B1	above D1	below C5	below D4
type	vhrst	vhrst	hag	hag	hbg	hbg
quartz	44.0	39.0	30.3	25.0	31.5	33.6
feldspar	1.3	2.0	4.8	2.0	3.0	2.4
VRF	0.0	0.0	0.0	0.0	0.0	0.0
SRF	4.3	1.0	1.0	8.0	15.5	6.3
MRF	0.3	0.0	0.0	0.0	0.0	0.0
porosity	5.6	7.0	2.0	1.0	5.0	3.6
authigenic dol	19.3	7.5	45.3	53.5	30.0	25.3
detrital calcite	3.3	2.5	2.0	0.0	0.0	3.6
undiff. clays	4.9	12.5	1.6	0.5	4.5	5.6
opaque grains	6.8	8.6	9.1	8.0	4.2	5.9
opaque matrix	10.2	19.9	3.9	1.0	4.2	13.7
opaque cement	0.0	0.0	0.0	1.0	2.1	0.0
total	100.0	100.0	100.0	100.0	100.0	100.0
grains	63.6	57.1	48.2	43.4	57.1	53.7
cement	20.4	8.1	46.2	55.1	33.8	26.2
matrix	16.0	34.8	5.6	1.5	9.2	20.0
total	100.0	100.0	100.0	100.0	100.0	100.0

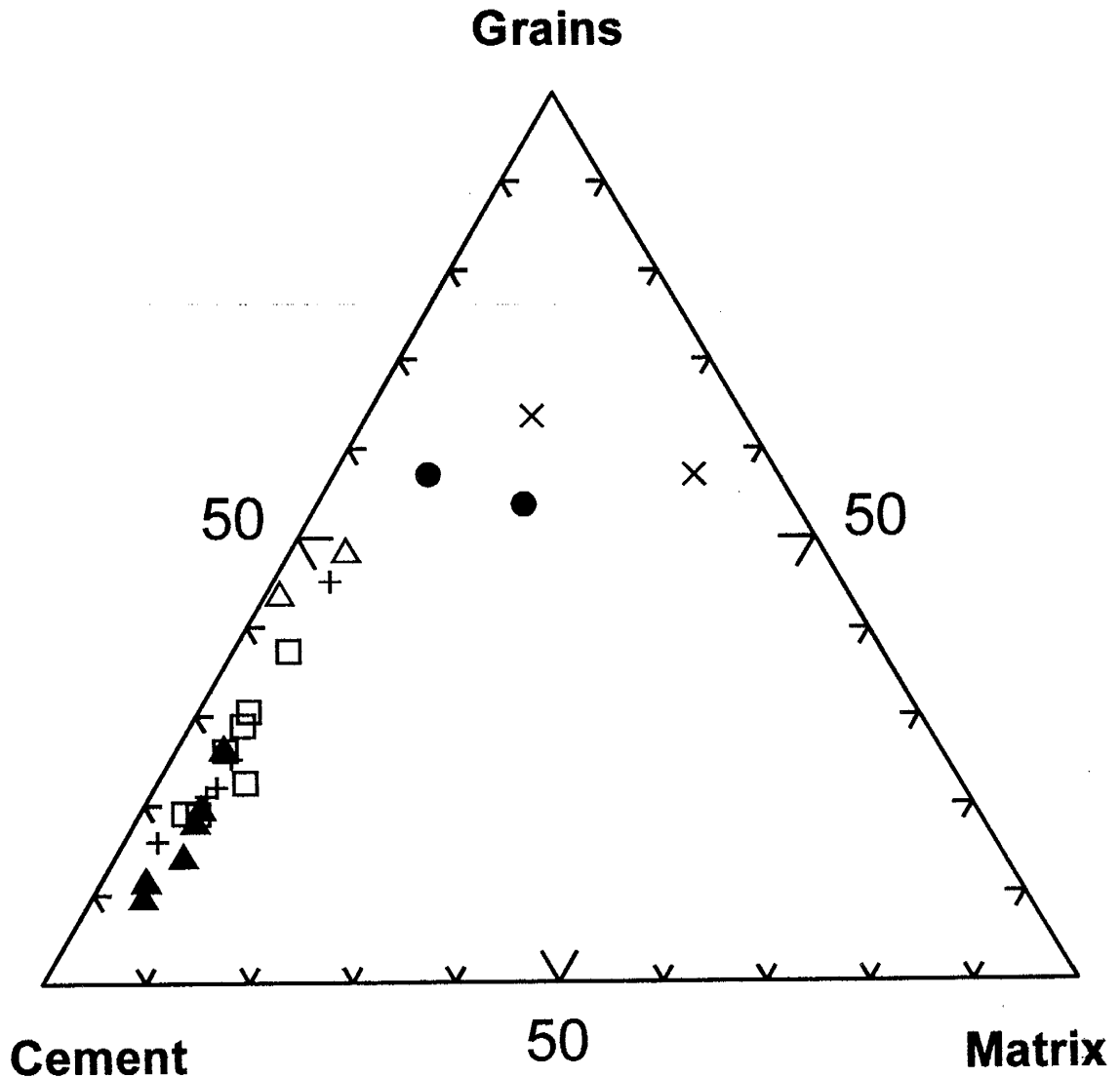
quantities than in the cemented zones, authigenic dolomite cement does occur in the host rock and accounts for between 8 and 54 volume percent.

Foraminifera tests comprise up to 4 percent of the host rock. Framework grains such as quartz, feldspar, opaque grains, and lithic fragments make up 43 to 57 percent of the host rock. Quartz varies in abundance from 25 to 44 percent and feldspar abundances vary from 2 to 5 percent. Lithic fragments (mainly chert) account for up to 16 percent, and opaque grains make up 4 to 9 percent of the host rock. Clay minerals and opaque matrix minerals account for up to 32 percent of the host rock, and porosity does not exceed 7 percent.

Figure 5 is a ternary diagram that summarizes the point-count data.

Cemented (grid) samples are grouped according to their relative vertical position. The categories 'core,' 'grid above core,' and 'grid below core' are based upon the spatial isotopic distribution within the individual grids (discussed in the next section). Host rock samples were divided into three categories: host above grid, host below grid, and vertical host rock traverse. In general, the cores (isotopically heaviest zones; see below) of the cemented zones contain the highest amount of cement by volume, and the grid samples above and below the cores contain slightly less cement than the cores. Host rock samples from the vertical sampling traverse have considerably more framework grains than the bulk of the grid samples and so plot closer to the top of the diagram. Host rock samples from above and below the grids are characterized by intermediate proportions of cement and grains.

Figure 5: Results of twenty-four 300-point point-counts.



- △ host above grid
- grid above core
- ▲ core
- + grid below core
- host below grid
- × vertical host rock traverse

Stable isotopic composition

The results of 324 stable isotopic analyses are summarized in Table 2. Figure 6 is a $\delta^{18}\text{O}$ - $\delta^{13}\text{C}$ cross-plot that features isotopic data from each of the grids. In addition, the spatial distribution of carbon and oxygen isotopes is shown on scaled contour diagrams of each grid in Figures 7-16. The host rock isotopic data is plotted in Figures 17-18.

Cemented (grid) samples

There is a strong linear correlation between carbon and oxygen isotopes in the dolomite cements of this study (Fig. 6). Each grid sample (regardless of areal location or stratigraphic depth) plots on or near a line ($R^2 = 0.984$) defined by $[\delta^{18}\text{O} = (0.5176) \delta^{13}\text{C} + 24.956]$. There is 20.4‰ of $\delta^{13}\text{C}$ variation (ranging from -9.7 to +10.7‰ PDB). $\delta^{18}\text{O}$ varies from 20.7 to 30.4‰ SMOW (-9.9 to -0.4‰ PDB).

Figures 7 through 16 show the spatial distribution of carbon and oxygen isotopes on scaled diagrams of each grid. The x and y coordinates of each of the plots are in centimeters (x is horizontal and y is vertical), and the oxygen and carbon isotopic data are contoured in the z direction. The “gunsite” symbols represent the relative locations of sampling drill holes, and the number beside or above each of the symbols is $\delta^{13}\text{C}$ or $\delta^{18}\text{O}$ expressed in permil relative to PDB or SMOW, respectively. The contour interval for each of the plots is one permil except where otherwise indicated.

Prairie Canyon Dolomites

Figure 6: $\delta^{13}\text{C}$ vs. $\delta^{18}\text{O}$ for all cemented (grid) samples.

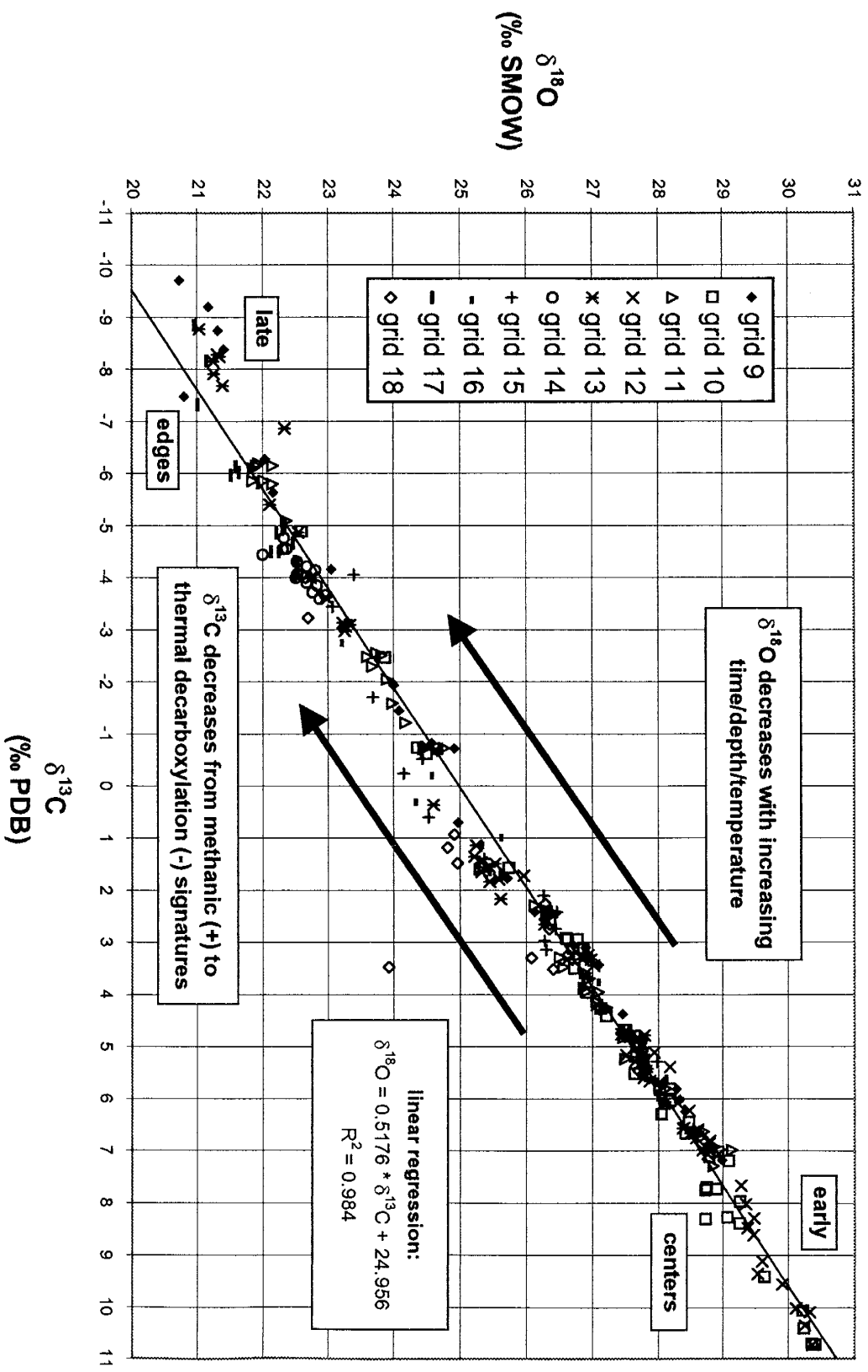


Figure 7: Stable isotope contour plots of Grid 9 samples. Grid 9 was sampled from the laterally continuous cemented horizon just below the top of Sequence D (same layer as Grids 11 and 13) at Area 2 (refer to Figure 4).

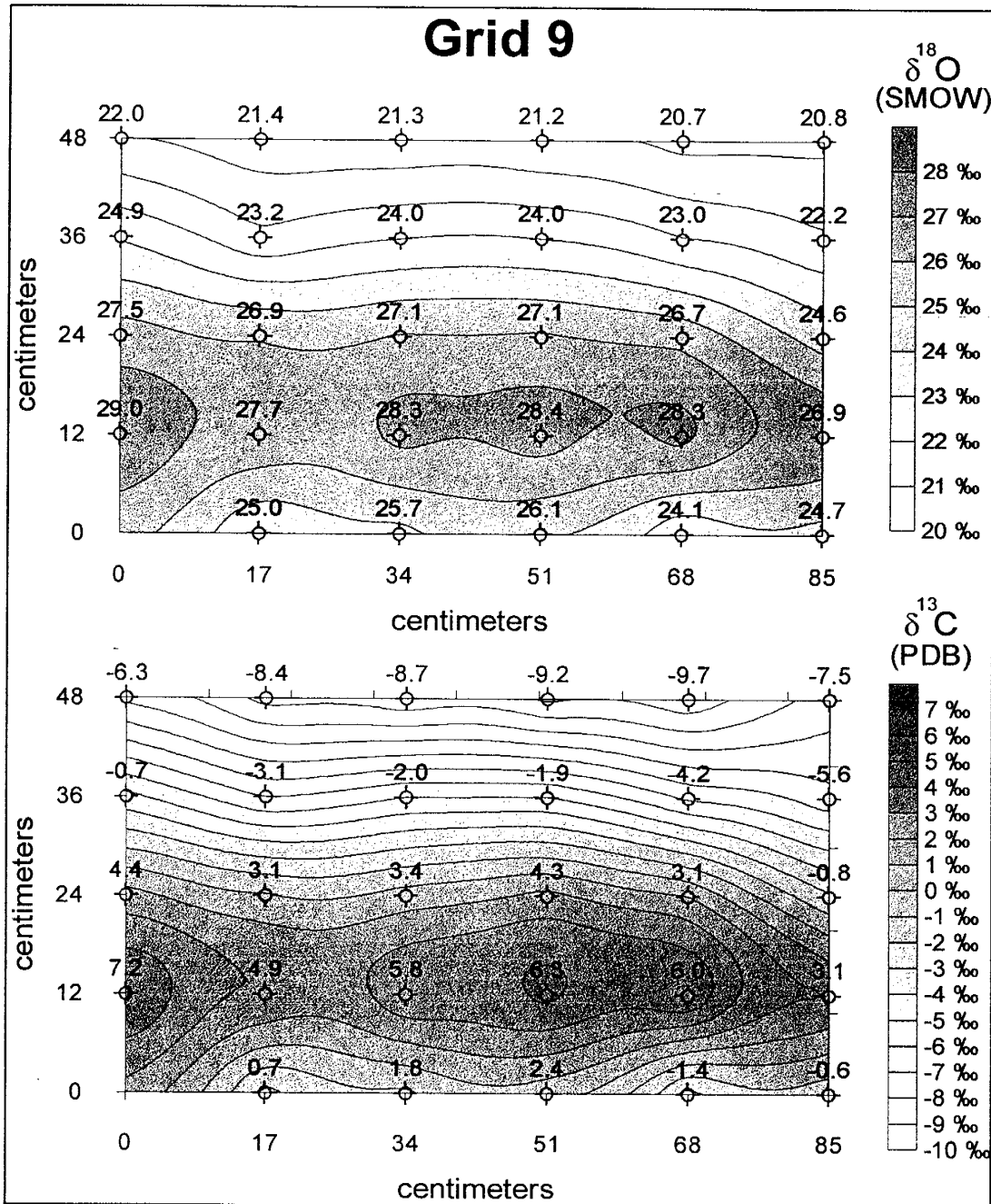


Figure 8: Stable isotope contour plots of Grid 11 samples. Grid 11 was sampled from the laterally continuous cemented horizon just below the top of Sequence D (same layer as Grids 9 and 13) at Area 4 (refer to Figure 4).

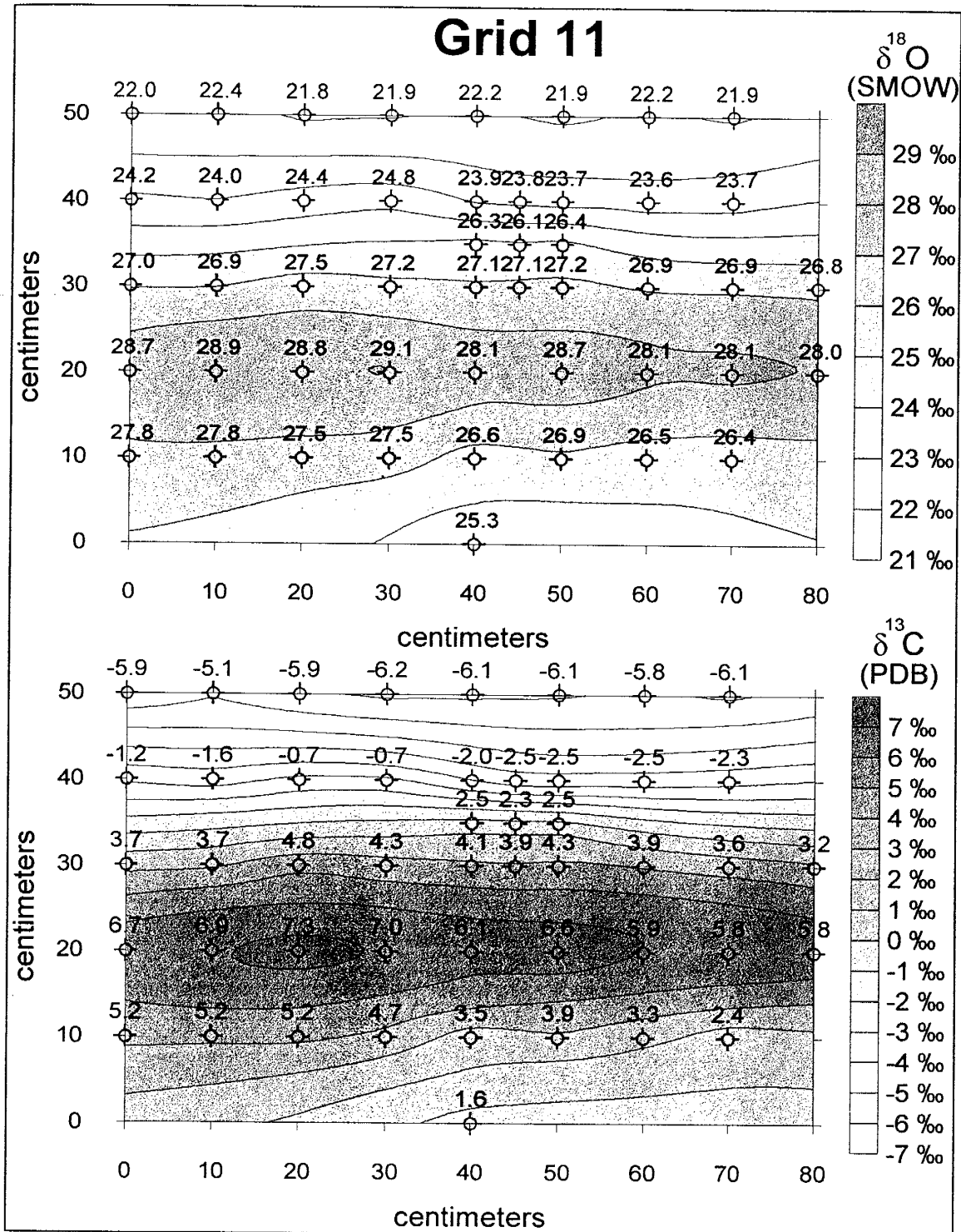


Figure 9: Stable isotope contour plots of Grid 13 samples. Grid 13 was sampled from the laterally continuous cemented horizon just below the top of Sequence D (same layer as Grids 9 and 11) at Area 4 (refer to Figure 4).

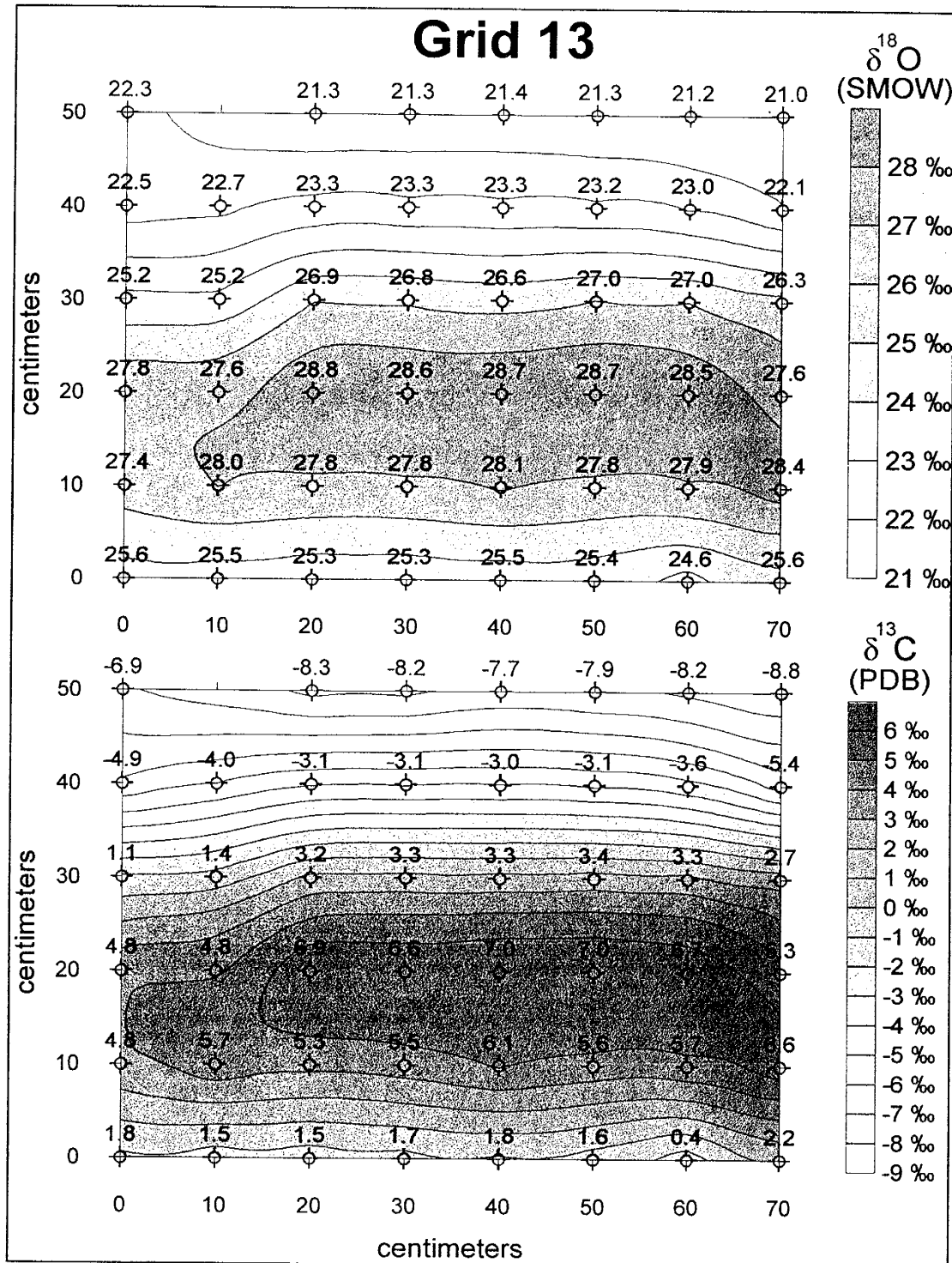


Figure 10: Stable isotope contour plots of Grid 15 samples. Grid 15 was sampled from the laterally continuous cemented horizon at the base of Sequence A (same layer as Grids 16 and 18) at Area 2 (refer to Figure 4).

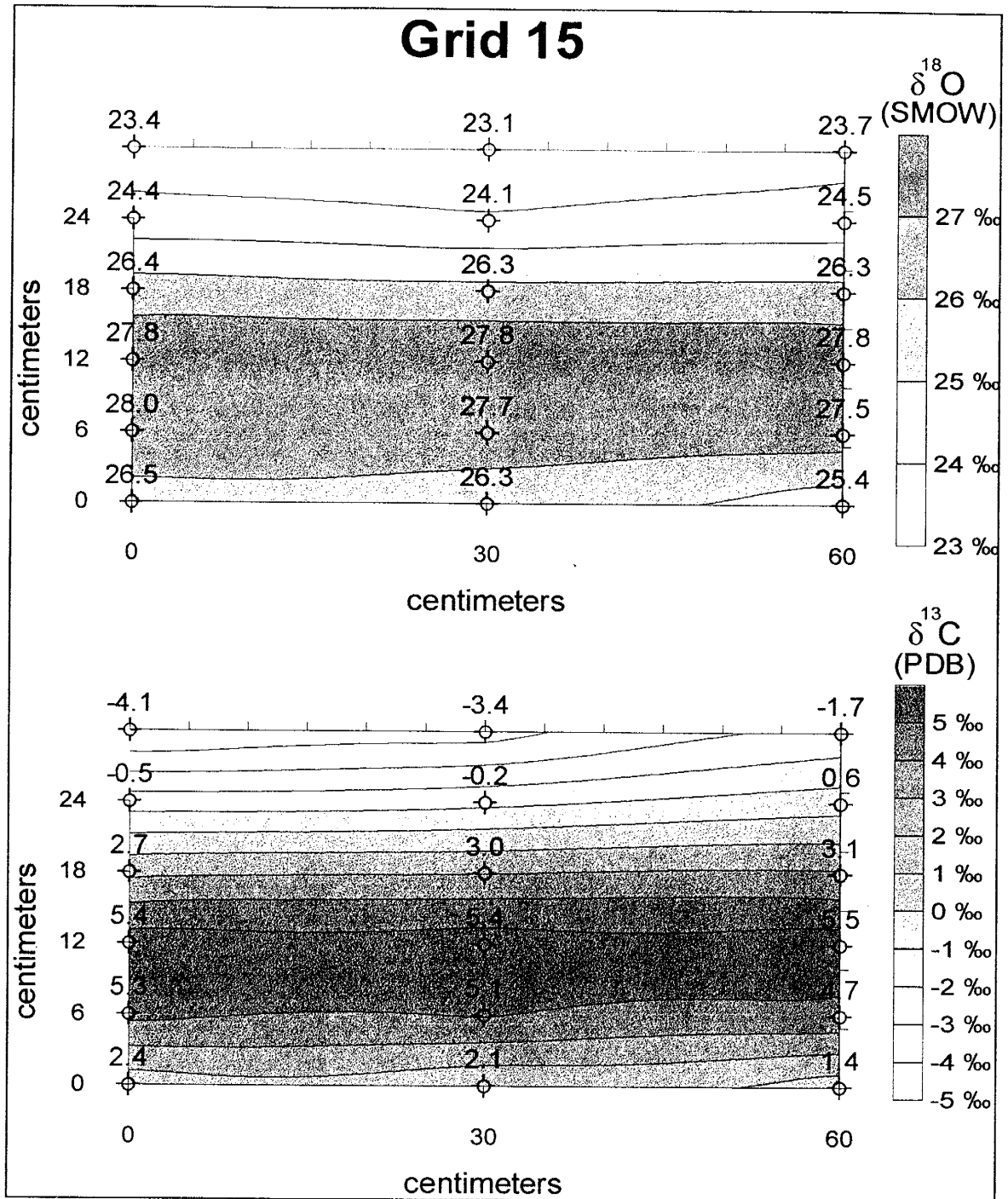


Figure 11: Stable isotope contour plots of Grid 16 samples. Grid 16 was sampled from the laterally continuous cemented horizon at the base of Sequence A (same layer as Grids 15 and 18) at Area 2 (refer to Figure 4).

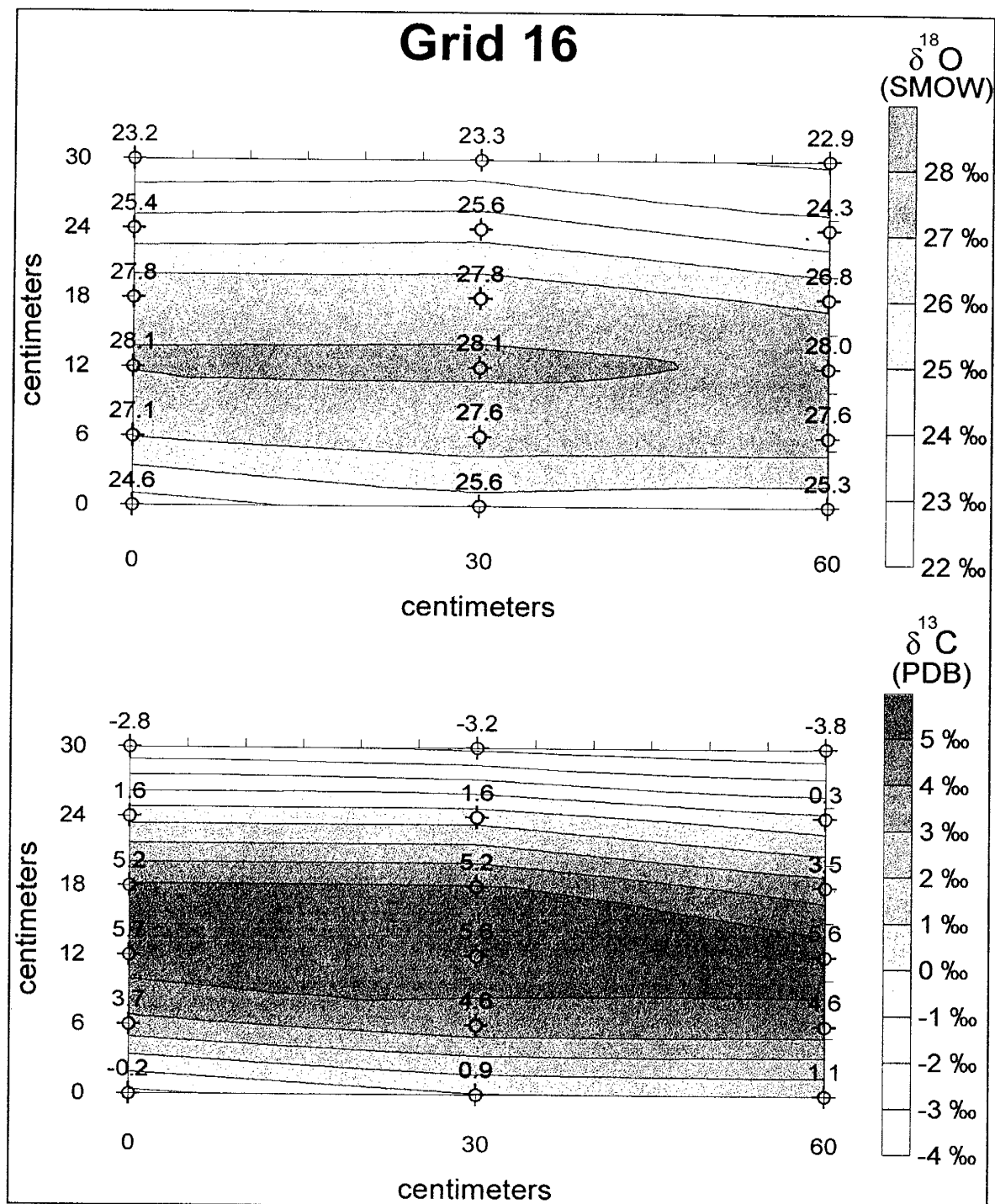


Figure 12: Stable isotope contour plots of Grid 18 samples. Grid 18 was sampled from the laterally continuous cemented horizon at the base of Sequence A (same layer as Grids 15 and 16) at Area 3 (refer to Figure 4).

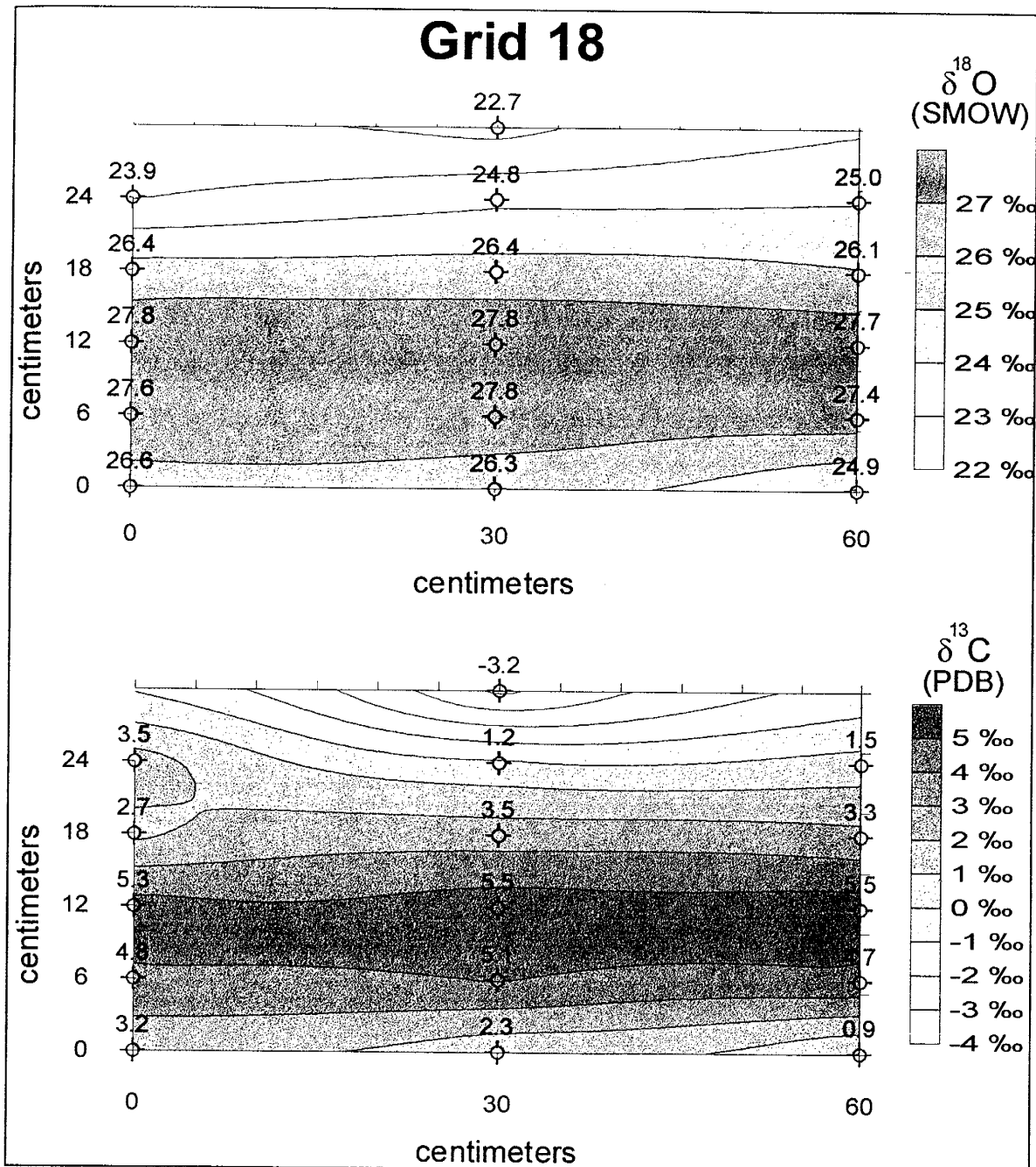


Figure 13: Stable isotope contour plots of Grid 10 samples. Grid 10 was sampled from the stratabound concretionary horizon at the top of Sequence D (same layer as Grid 12) at Area 2 (refer to Figure 4).

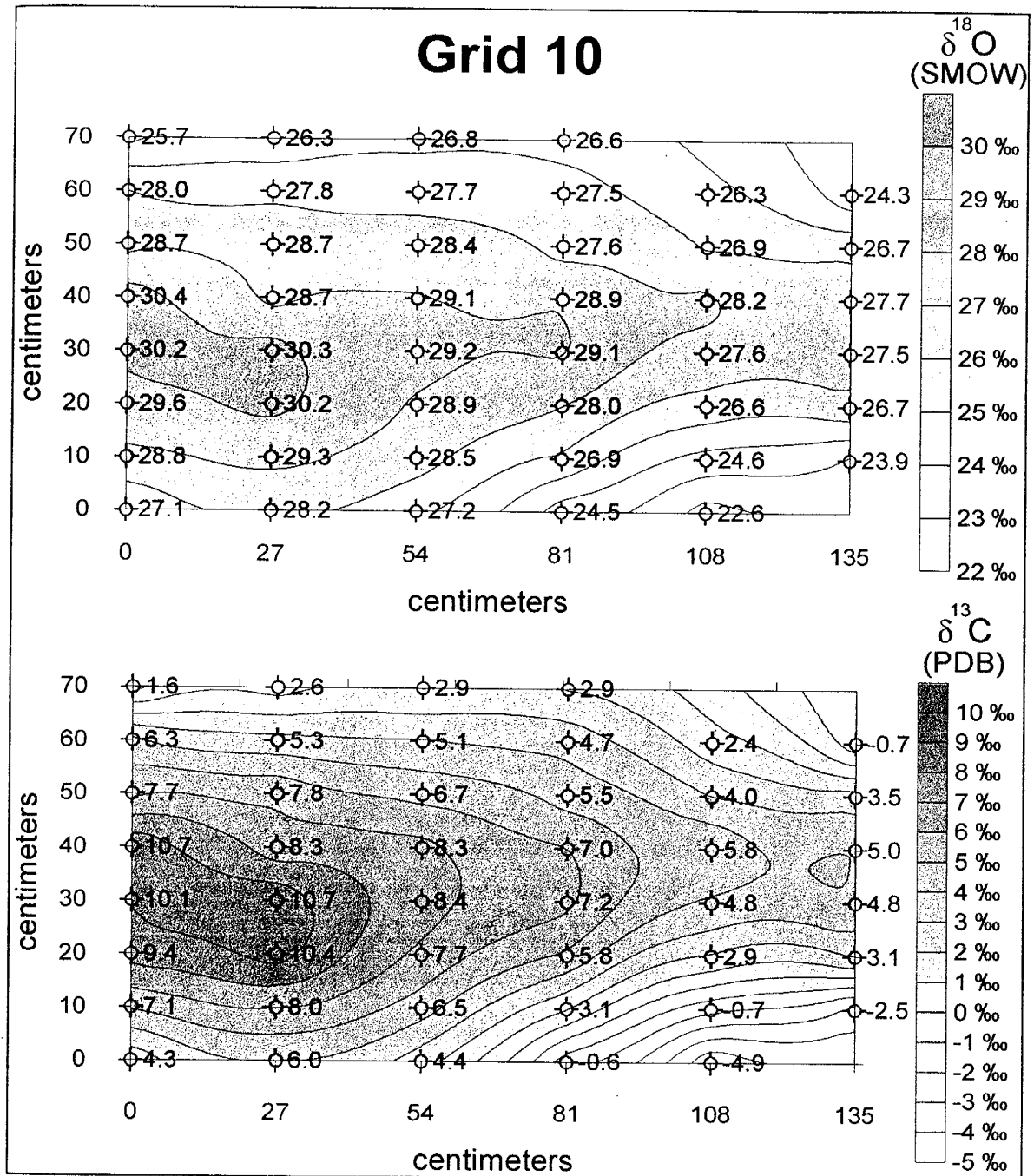


Figure 14: Stable isotope contour plots of Grid 12 samples. Grid 12 was sampled from the stratabound concretionary horizon at the top of Sequence D (same layer as Grid 10) at Area 4 (refer to Figure 4).

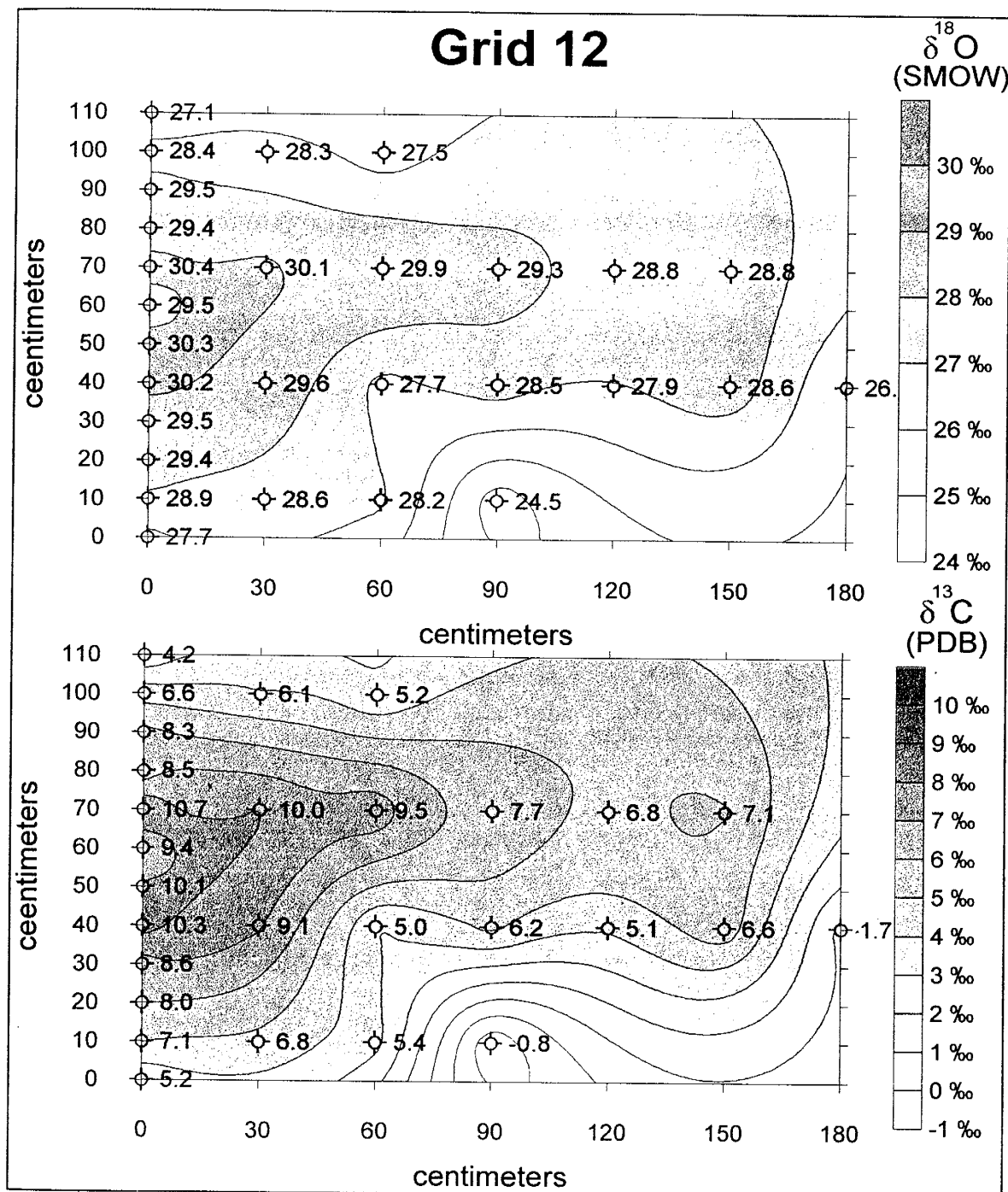


Figure 15: Stable isotope contour plots of Grid 14 samples. Grid 14 was sampled from the stratabound concretionary horizon at the top of Sequence C at Area 2 (refer to Figure 4). **Note:** Cont. Int. = 0.1 ‰ (both diagrams).

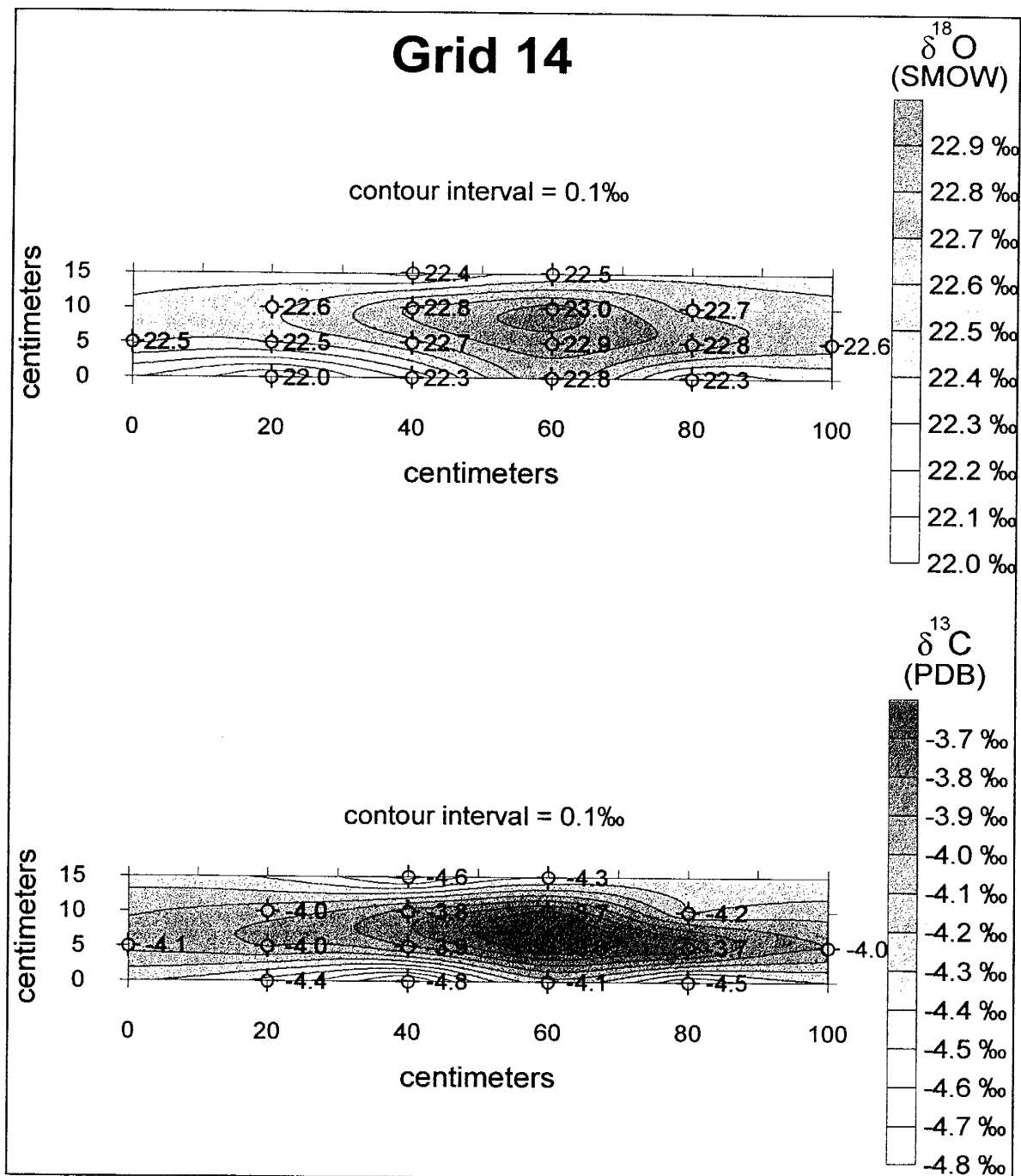
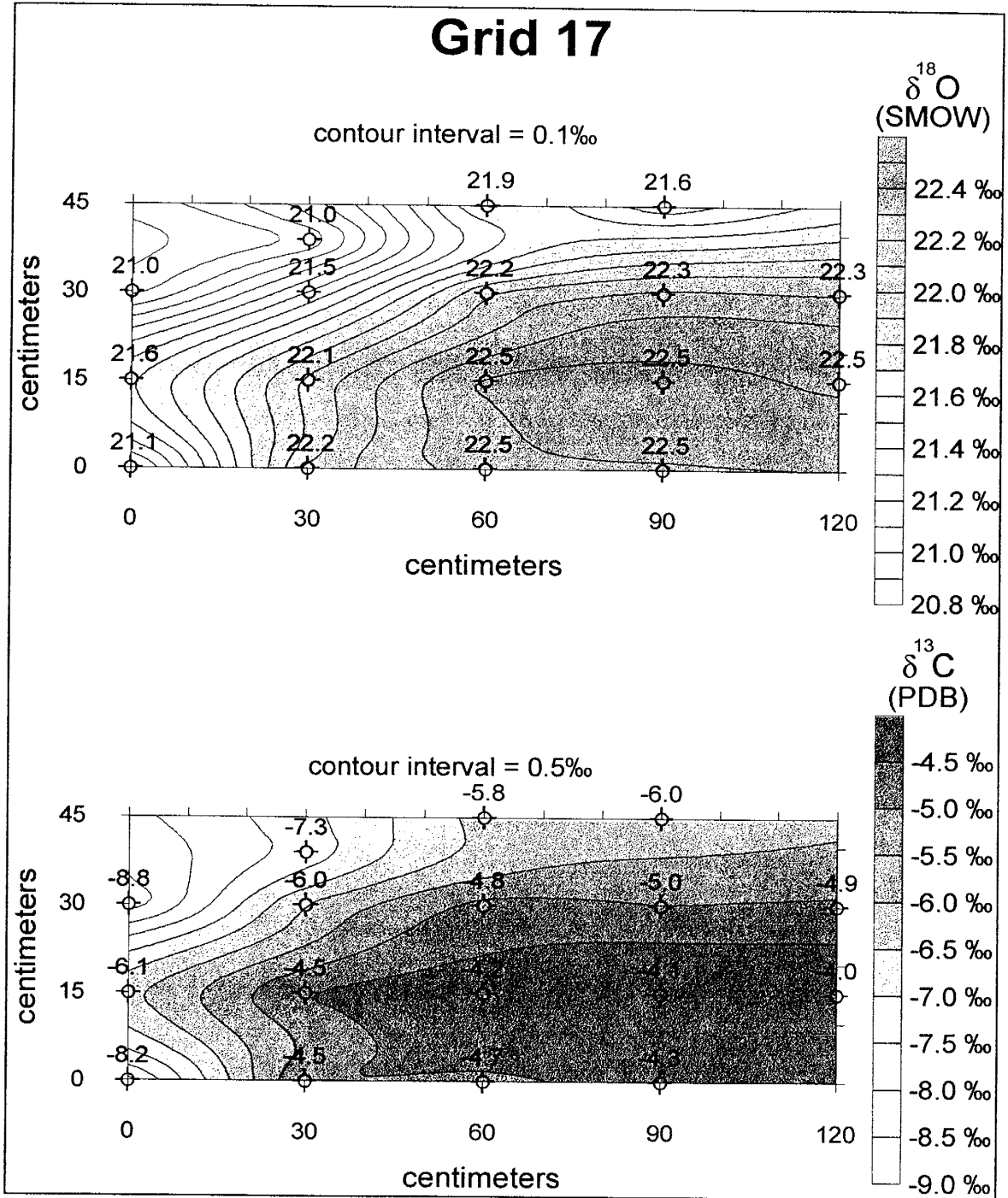


Figure 16: Stable isotope contour plots of Grid 17 samples. Grid 17 was sampled from the stratabound concretionary horizon at the top of Sequence B at Area 2 (refer to Figure 4). **Note:** contour interval = 0.1 ‰ (oxygen) and 0.5 ‰ (carbon).



In general, the heaviest $\delta^{18}\text{O}$ and $\delta^{13}\text{C}$ values occur in the cores (centers) of the cemented zones, and the values decrease toward the edges. The isotopically heavy cores of the two continuously cemented horizons (Sequence D: Grids 9, 11, 13; Sequence A: Grids 15, 16, 18) are situated below the physical centers of the layers, and the lightest values in these two horizons occur at the upper margins (Figs. 7-12). In contrast, the heavy cores of the concretions typically occur at their geometric centers. Isotopic variation is greater in the vertical direction than in the horizontal direction in all of the grids, but concretions (Grids 10, 12, 14, and 17; Figs. 13-16) tend to have more horizontal variation than the laterally continuous cemented layers (Figs. 7-12).

Sequence D (continuous layer)

Grids 9, 11, and 13 (Figs. 7, 8, and 9) were collected at different outcrops of the continuously cemented horizon situated just below the top of Sequence D. Grid 9 is from Area 2, and Grids 11 and 13 are from Area 4, 1.5 km away. Grid 11 is located 2.3 meters to the right of Grid 13.

Grid 9 (Fig. 7) has 29 samples that are spaced 17 cm apart laterally and 12 cm apart vertically. $\delta^{18}\text{O}$ values range from 20.7‰ at the top of the grid to 29.0‰ at the core, and $\delta^{13}\text{C}$ values range from -9.7‰ to +7.2‰. There is more horizontal isotopic variation (in both isotopes) at the core of Grid 9 than at either the upper or the lower edges.

There are forty-eight samples in Grid 11 (Fig. 8). The main grid has 43 samples that are spaced 10 cm apart in both the horizontal and vertical

directions. In addition, five more samples were analyzed from a subgrid (5 cm spacing) near the top and center of Grid 11. $\delta^{18}\text{O}$ ranges from 21.8‰ at the top of the grid to 29.1‰ at the core, and $\delta^{13}\text{C}$ values range from -6.2 to +7.3‰. Like Grid 9, there is more carbon and oxygen isotopic variation in the horizontal direction at the core of Grid 11 than at either the upper or lower margins of the grid.

Grid 13 (Fig. 9), located 2.3 meters to the left of Grid 11, has 47 samples spaced 10 cm apart in both the horizontal and vertical directions. $\delta^{18}\text{O}$ values range from 21.0‰ at the top of the grid to 28.8‰ at the core, and $\delta^{13}\text{C}$ ranges from -8.8‰ (top) to +7.0‰ (core). There is more horizontal isotopic variation (in both isotopes) at the core of Grid 13 than at either the upper or the lower edges.

Sequence A (continuous layer)

Grids 15, 16, and 18 (Figs. 10, 11, and 12) are from the continuous layer at the base of Sequence A. Grid 15 is situated 17.6 m left (west) of Grid 16 at Area 2, and Grid 18 is located at Area 3, 1.0 km to the southeast. All three grids have a 30cm x 6cm grid spacing. Because of the lower sampling density in the horizontal direction of these grids, it is not possible to tell whether or not there is more horizontal isotopic variation at the cores than at the outer margins.

Grid 15 (Fig. 10) is comprised of three columns of six samples each. $\delta^{18}\text{O}$ values range from 23.1‰ at the top of the grid to 28.0‰ at the core. Carbon values range from -4.1 (top) to +5.5‰ (core).

Grid 16 (Fig. 11) features 18 samples from three columns. It has 5.2‰ of $\delta^{18}\text{O}$ variation with values ranging from 22.9‰ at the top to 28.1‰ at the core. $\delta^{13}\text{C}$ values increase from -3.8‰ at the top to 5.7‰ at the core (9.5‰ total variation).

Grid 18 (Fig. 12) is made up of sixteen samples collected from three columns. The middle column has six sample points, and the left and right columns each contain five samples. The upper samples of the left and right columns could not be attained because part of the top of the outcrop had been removed by erosion. $\delta^{18}\text{O}$ values range from 22.7‰ at the top of the grid to 27.8‰ at the core (5.1‰ total change). Grid 18 has 8.7‰ of $\delta^{13}\text{C}$ variation with values ranging from -3.2 (top) to 5.5‰ (core).

Sequence D (concretions)

Grids 10 and 12 (Figs. 13 and 14) are from two stratabound concretions at the top of Sequence D. Grid 10 (Area 2) is 1.5 km away from Grid 12 (Area 4) in the same discontinuous layer. The left sides of both grids bisect the cores of the concretions from which they originated, and the heaviest (core) delta values for both isotopes are identical in both grids. Carbon and oxygen isotopic contours show a general concentric decrease away from the concretion cores, and a number of the contours show closure toward the right margins of the diagrams.

Grid 10 (Fig. 13) has 45 samples that are spaced 27 cm apart horizontally and 10 cm apart vertically. There is 7.8‰ of variation in $\delta^{18}\text{O}$ with values

ranging from 22.6‰ (lower right) to 30.4‰ at the core. Grid 10 boasts 15.6‰ of $\delta^{13}\text{C}$ variation with values ranging from -4.9‰ (lower right) to +10.7‰ (core). There is more horizontal isotopic variation (in both isotopes) at the core of Grid 10 than at either the upper or the lower edges.

Grid 12 (Fig. 14), located 1.5 km to the northeast of Grid 10, has 28 samples. The grid has a 30cm x 30cm spacing (horizontally and vertically) except for the left column which has a 10 cm vertical spacing. Oxygen isotope delta values range from 24.5‰ (lower right) to 30.4‰ at the core, and $\delta^{13}\text{C}$ ranges from -0.8 (lower right) to +10.7‰ (core).

Sequence C (concretion)

Grid 14 (Fig. 15) of Area 2 is a small isolated concretion from the discontinuous horizon that caps Sequence C. Samples were collected at 20 cm intervals in the horizontal direction and 5 cm intervals in the vertical direction. The entire concretion is only one meter long and 15 cm high so the grid covers an entire cross-section of the concretion. Both isotopes have maximum values at the center (core) of the concretion, but note that the contour interval is only 0.1‰ (both isotopes) on Figure 15. There is only 1‰ of variation in $\delta^{18}\text{O}$ at Grid 14 with values ranging from 22.0 to 23.0‰. There is 1.2‰ variation in $\delta^{13}\text{C}$ with values ranging from -4.8 to -3.6‰.

Sequence B (concretion)

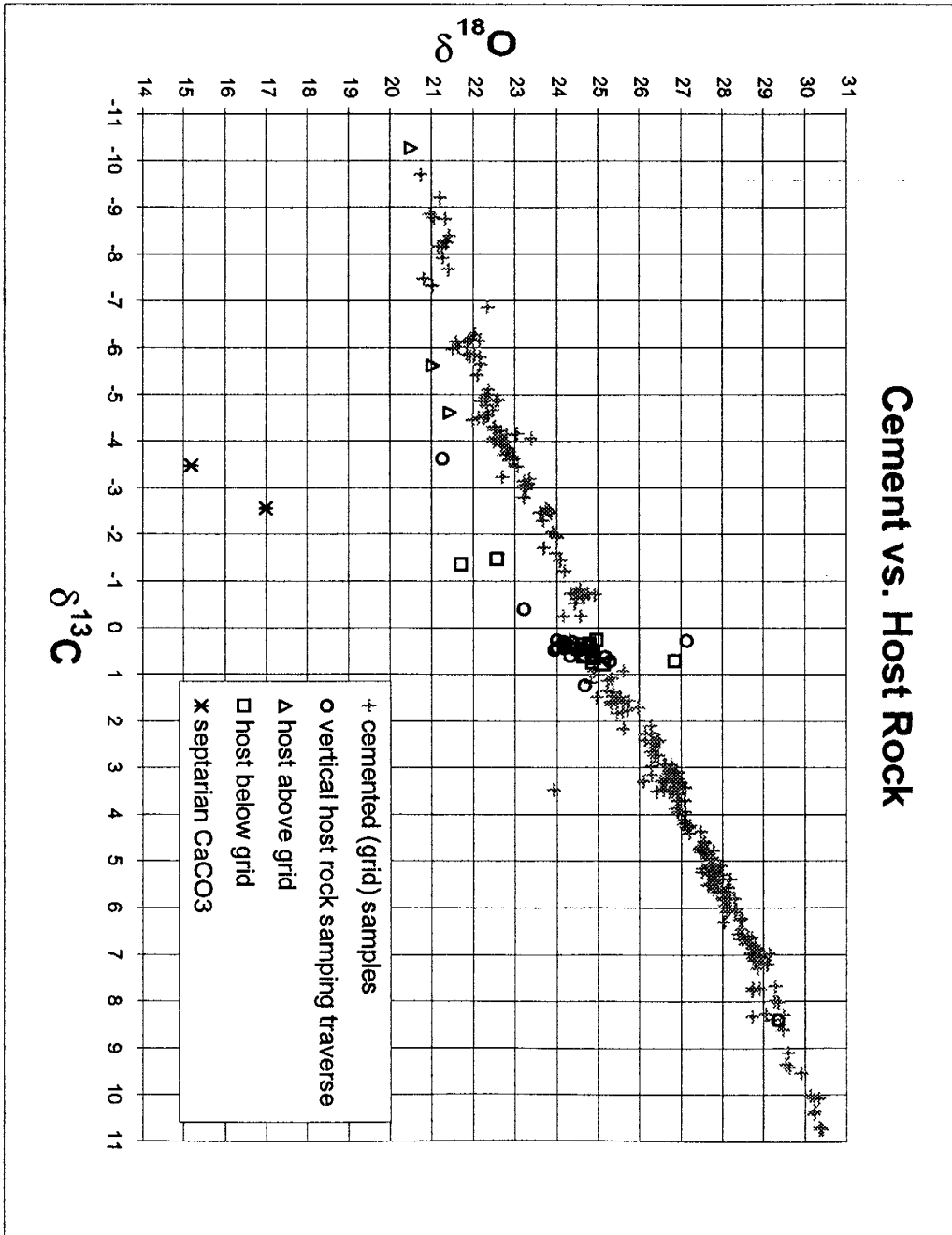
Grid 17 (Fig. 16) of Area 2 is an isolated concretion from the discontinuous horizon that caps Sequence B. Samples were collected at 30 cm intervals in the horizontal direction and 15 cm intervals in the vertical direction. The right side of the grid bisects the core of the concretion. Both isotopes have maximum values at the center (core) of the concretion. However, note that the contour interval is only 0.1‰ for oxygen and 0.5‰ for carbon on Figure 16. There is 1.5‰ variation in $\delta^{18}\text{O}$ at Grid 17 with values ranging from 21.0 to 22.5‰. $\delta^{13}\text{C}$ values range from -8.8 to -4.0‰ (4.8‰ total variation).

Host rock samples

Figure 17 shows the relationship of the host rock samples to the grid samples in $\delta^{13}\text{C}$ - $\delta^{18}\text{O}$ space. The host rock samples are divided into three categories, based on where they were collected: host above grid, host below grid, and vertical host rock sampling traverse. This nomenclature is consistent with that used in the discussion of the point-count and microprobe data. However, there do not seem to be any significant differences in the isotopic behavior of the host rock among these three groups. Therefore, the term 'host rock' applies to these three groups collectively.

There is some scatter in the host rock data, but most of the points occur on or below the line formed by the dolomite-cemented samples between $23.5\text{‰} < \delta^{18}\text{O} < 25.5\text{‰}$ and $0\text{‰} < \delta^{13}\text{C} < 1\text{‰}$ (Fig. 17). Two host rock samples plot above the line, and several more samples plot below the dolomite cement line

Figure 17: Cemented samples vs. host rock. Septarian calcite also shown.



with $-6\text{‰} < \delta^{13}\text{C} < 0\text{‰}$. One of the 'host above grid' samples is the isotopically lightest sample (with respect to carbon) and plots at the lower left end of the cement line. One of the 'vertical host rock sampling traverse' samples plots near the upper right (isotopically heaviest) end of the line and appears to be an outlier from the rest of the host rock samples.

Figure 18 shows the variation in $\delta^{13}\text{C}$ with depth along the vertical host rock sampling traverse which begins at the base of Sequence C (above Grid 17) and ends just above the top of Sequence D. Almost all of these samples lie within the range $0\text{‰} < \delta^{13}\text{C} < 1\text{‰}$. However, there are wild fluctuations within the upper 20 feet of Sequence D below its two cemented horizons. Within a twenty foot interval, $\delta^{13}\text{C}$ values decrease to -3.6‰ , increase to $+8.4\text{‰}$, and then return to more average values (near 0‰).

The results of two analyses of calcite veins from the cores of septarian concretions at Grids 10 and 12 are also shown on Figure 17. The two grids are located 1.5 kilometers apart from each other. The septarian calcite plots well below the dolomite cement line with $-3.5\text{‰} < \delta^{13}\text{C} < -2.5\text{‰}$ and $15\text{‰} < \delta^{18}\text{O} < 17\text{‰}$. These are the most ^{18}O -depleted values in the data set.

Elemental composition

The results of 103 microprobe analyses from nine samples are presented in Table 4. One host rock sample and eight cemented (grid) samples were analyzed. Four of the eight grid samples are from a vertical traverse through Grid 11. The remaining four are samples of the cores and edges of Grid 10

Figure 18: Carbon isotopic variation with depth along the vertical host rock sampling traverse (vhrst).

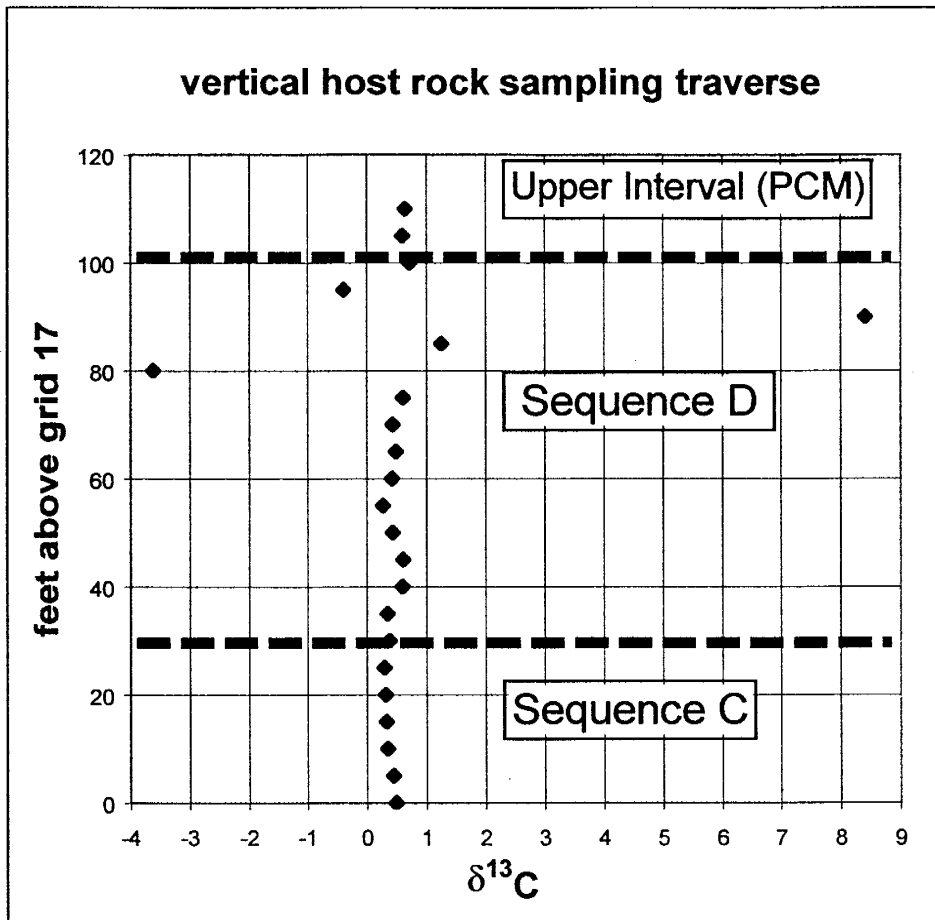


Table 4: Microprobe results.

sample	BSE	type	FeCO ₃	CaCO ₃	MgCO ₃
G11-A2	light	edge	7.88	55.22	36.90
G11-A2	dark	edge	1.09	48.85	50.06
G11-A2	light	edge	7.82	55.15	37.03
G11-A2	dark	edge	0.65	49.99	49.36
G11-A2	light	edge	8.02	54.41	37.57
G11-A2	dark	edge	0.26	53.49	46.25
G11-A2	light	edge	8.76	52.67	38.57
G11-A2	dark	edge	0.47	50.97	48.56
G11-A2	dark	edge	7.22	54.55	38.24
G11-A2	dark	edge	3.14	51.62	45.24
G11-A2	light	edge	8.43	54.52	37.05
G11-A2	dark	edge	0.67	51.04	48.29
G11-A2	light	edge	7.98	52.97	39.05
G11-A3	dark	edge	0.55	50.30	49.15
G11-A3	light	edge	4.45	56.02	39.53
G11-A3	light	edge	4.21	55.42	40.37
G11-A3	dark	edge	0.36	49.39	50.25
G11-A3	light	edge	4.54	53.69	41.77
G11-A4	dark	core	6.11	55.31	38.59
G11-A4	light	core	10.66	54.03	35.32
G11-A4	dark	core	2.63	51.28	46.09
G11-A4	light	core	9.33	55.62	35.04
G11-A4	dark	core	6.03	53.16	40.81
G11-A4	light	core	9.26	53.95	36.80
G11-A4	dark	core	5.33	52.30	42.37
G11-A4	light	core	7.07	53.92	39.02
G11-A4	dark	core	4.38	53.51	42.12
G11-A4	dark	core	4.96	53.29	41.76
G11-A4	dark	core	1.54	51.80	46.65
G11-A4	light	core	8.15	52.89	38.96
G11-A4	dark	core	4.84	52.52	42.64
G11-A4	light	core	3.75	55.21	41.04
G11-A4	dark	core	4.32	51.91	43.77
G11-A4	light	core	3.80	54.36	41.84
G11-A5	dark	edge	0.03	52.22	47.74
G11-A5	light	edge	5.74	53.83	40.43
G11-A5	light	edge	5.13	55.44	39.43
G11-A5	dark	edge	0.22	51.71	48.06
G11-A5	dark	edge	0.03	50.10	49.87
G11-A5	light	edge	5.63	53.35	41.03
G11-A5	dark	edge	0.23	49.45	50.32
G11-A5	light	edge	4.75	52.15	43.10
G18-A4	light	core	5.37	52.18	42.45
G18-A4	light	core	3.72	49.93	46.35
G18-A4	light	core	14.67	54.11	31.23
G18-A4	dark	core	0.12	49.73	50.16
G18-A4	light	core	6.43	51.88	41.69
G18-A4	light	core	5.86	53.00	41.14
G18-A4	light	core	6.18	49.24	44.58
G18-A4	dark	core	1.80	49.59	48.61
G18-A4	light	core	6.65	48.84	44.51

(Sequence D, concretion) and Grid 18 (Sequence A, continuous layer). One host rock sample was analyzed: sample S6 from the vertical host rock sampling traverse.

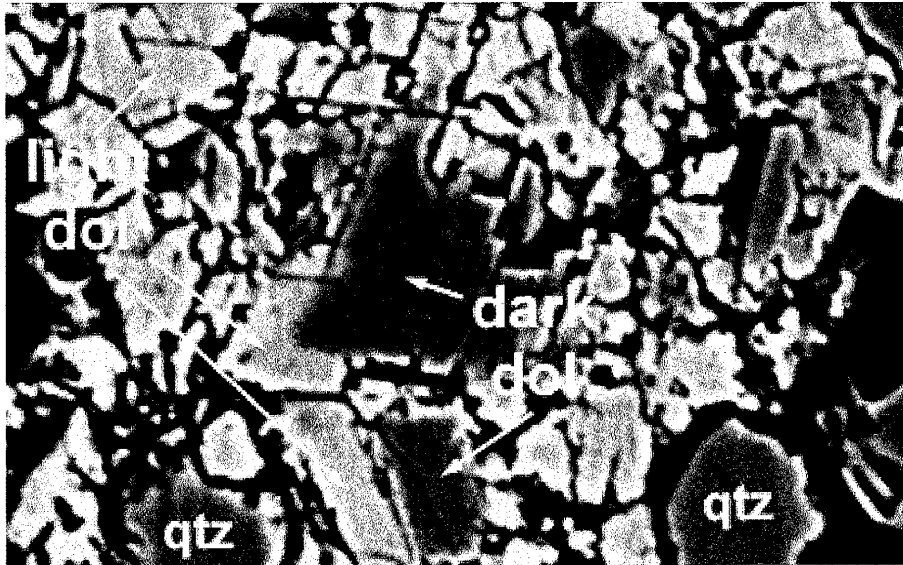
Two compositionally distinct generations of cement are apparent in back-scattered electron (BSE) images of all the cemented (grid) samples (Fig. 19a). A dark, low-Fe dolomite preceded a lighter colored, more Fe-rich cement. This temporal relationship is evidenced by the fact that the lighter cement surrounds the dark material. There is a bimodal distribution in the chemistries of these two generations of cement (Fig. 19b). The iron content of the early (dark) cement ranges from end-member dolomite composition (no iron) to ferroan dolomite (approximately 6% Fe). The lighter colored cement has between 4 and 15% iron. Some of the light colored cements classify as ankerite.

Figure 20 shows the microprobe data plotted as core samples versus edge samples. The designations are based upon the isotope patterns (Figs. 7-16), and 'edge' refers to samples that are either above or below an isotopically heavy core. Both core and edge samples span the entire compositional range of the cements, but the most ankeritic cements occur in the core of Grid 18.

There appears to be no significant difference in the proportion of light and dark cements between the cores and edges of the cemented layers (Figs. 19b and 20). A vertical traverse (top edge to core to bottom edge) of four Grid 11 samples (Sequence D, continuous) has a consistent ratio of light cement to dark cement of approximately five to one as indicated by point-counts of digital BSE photomicrographs.

Figure 19: Microprobe results. (a) Two generations of dolomite cement were evident in back scattered electron images. A dark, Fe-poor dolomite cement preceded the lighter, more ferroan cement as is evidenced by the fact that the light cement surrounds the dark cement. Bright areas are edge effects and do not reflect compositional variation. (b) Some of the ferroan material is ankeritic in composition. Both the dolomite and the calcite in the host rock have end-member compositions.

(a)



(b)

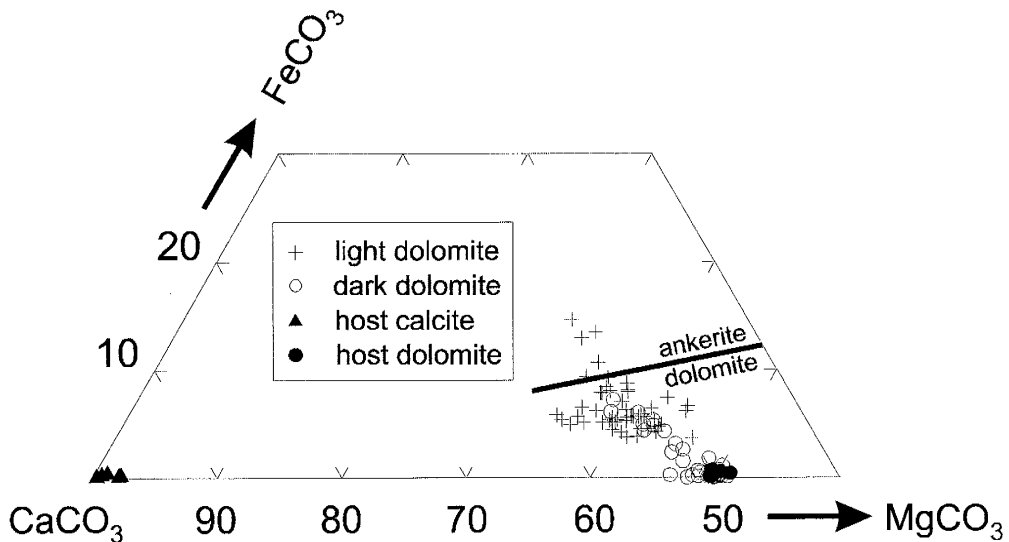
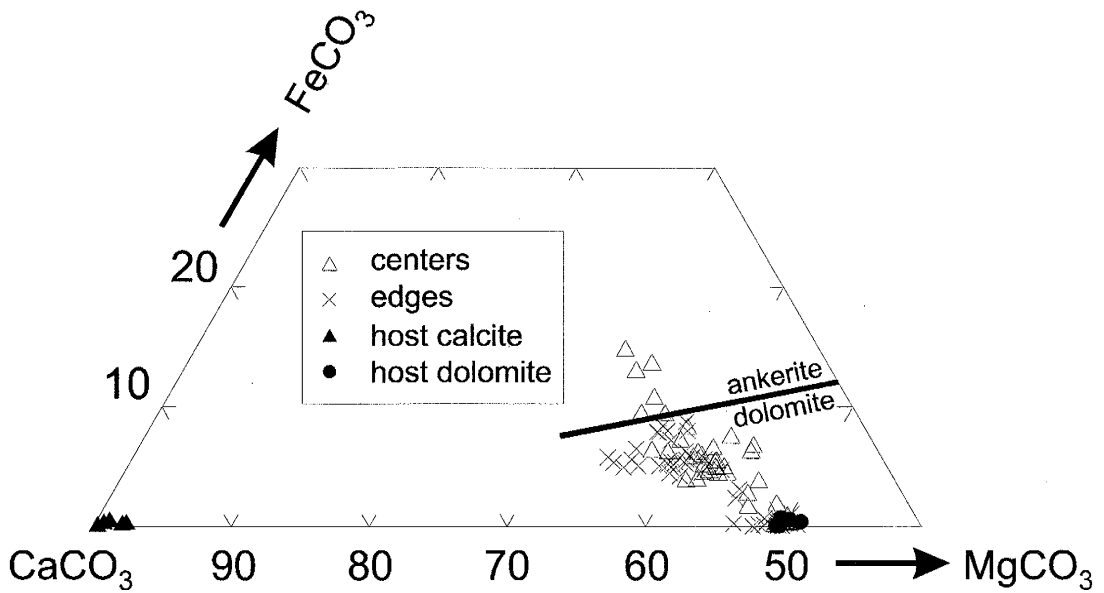


Figure 20: Both core and edge samples of each grid span the range of dolomite cement chemistries. However, the most Fe-rich (ankeritic) cements were found in the core of Grid 18.



The one host rock sample (sample S6) that was analyzed contains calcite and dolomite (Figs. 19b and 20). The microprobe analyses show that both of these carbonates have end-member compositions. The host rock dolomite is dark in BSE images and is similar in appearance and composition to the low-Fe, early-stage dolomite in the grid samples.

DISCUSSION

Several questions need to be answered in order to make meaningful inferences about the spatial and temporal distribution of carbon and oxygen isotopes in the Prairie Canyon dolomites. For example, how, when, and under what thermal and microbiological conditions did the Prairie Canyon cements form? What caused the isotopic zonation at the outcrop (mesoscopic) scale (Figs. 7-16)? Are the observed zonations persistent over large (macro- to megascopic) intervals? A satisfactory interpretation will also need to explain the coupled fractionation of both carbon and oxygen isotopes (Fig. 6) through time, and account for the high minus-cement porosities of the Prairie Canyon dolomites.

$\delta^{18}\text{O}$ values in temperature-depth calculations

Numerous authors (e.g., Irwin et al., 1977; Hennessy and Knauth, 1985; and others) have used $\delta^{18}\text{O}$ of carbonate minerals as a proxy measure of burial depth because of its temperature dependence. If pore-water $\delta^{18}\text{O}$ is assumed to

be constant, the heaviest $\delta^{18}\text{O}$ values should correspond to the lowest temperatures of precipitation and therefore the shallowest burial depths. Lighter values should represent higher temperatures and greater depths (Kelts and McKenzie, 1982). However, several uncertainties are associated with temperature and depth calculations. For instance, it is necessary to assume a pore-water $\delta^{18}\text{O}$, a geothermal gradient, and a bottom water temperature. Further, it is necessary to know the temperature dependent fractionation for the dolomite-water system (there are several available; see below).

The $\delta^{18}\text{O}$ values of the Prairie Canyon dolomites vary from 20.7 to 30.4‰ (SMOW). If the pore-water $\delta^{18}\text{O}$ was constant, these values could correspond to precipitation temperatures of between 24 and 84°C (assuming a Cretaceous seawater $\delta^{18}\text{O}$ of -1.2‰ SMOW; Shackleton and Kennett, 1975). Conversely, if temperature is assumed to have been a constant 5°C (reasonable for marine bottom waters), this range of $\delta^{18}\text{O}$ values may represent a range of pore-water $\delta^{18}\text{O}$ compositions from -15.4 to -5.7‰ (SMOW). The fractionation relationship of Fritz and Smith (1970) was chosen for these calculations because it is calibrated for temperatures typical of diagenetic environments (25-78°C). However, it yields slightly lower temperatures than the relationships of Northrop and Clayton (1966), O'Neil and Epstein (1966), or Land (1983) given the same dolomite $\delta^{18}\text{O}$ values and pore-water composition.

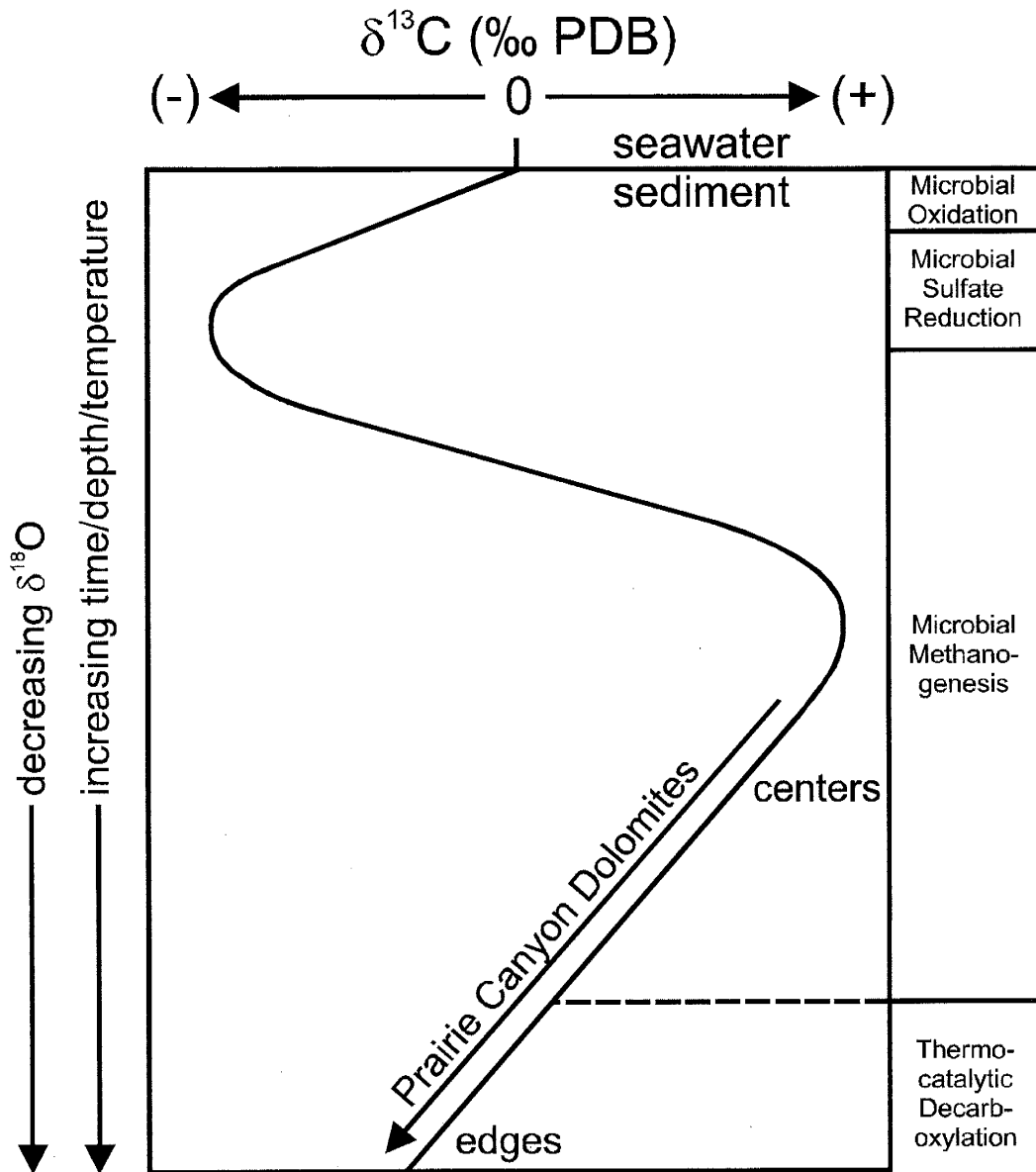
Assuming a linear geothermal gradient of 30°C/km and a bottom water temperature of 5°C, these temperatures (24-84°C) correspond loosely to

precipitation depths of between 0.6 and 2.6 kilometers. Although these are not unreasonable temperatures or burial depths, textural evidence suggests that these cements began to form early (i.e., at shallow depths) rather than late in the diagenetic history of the sediment. The point-count data indicates a higher minus-cement porosity (upwards of 80%) in the cemented (grid) samples than in the surrounding host rock (8-55%). This suggests that the concretions and laterally extensive horizons of the Middle Interval of the PCM formed prior to significant compaction (i.e., early in the sediment's diagenetic history). If this was the case, why are the oxygen isotope temperatures so high? Several processes will be evaluated later in this discussion that could have caused the depleted $\delta^{18}\text{O}$ values (and correspondingly high oxygen isotope temperatures).

$\delta^{13}\text{C}$ as an indicator of organic diagenesis

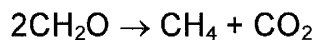
Like $\delta^{18}\text{O}$, carbon isotopic signatures are useful for understanding the timing and depth of precipitation of authigenic carbonates (Irwin, et al., 1977; Hennessy and Knauth, 1985; Baker and Burns, 1985; and others). There are four main diagenetic reaction zones that occur at various depths in the sediment column (Fig. 21). In each of the zones, CO_2 is generated as a by-product of organic matter degradation. Listed downward from the sediment-water interface, the individual zones are (1) microbial oxidation; (2) microbial sulfate reduction; (3) microbial methanogenesis (fermentation); and (4) thermocatalytic decarboxylation (Claypool and Kaplan, 1974). The actual depth and thickness

Figure 21: Depth stratified $\delta^{13}\text{C}$ variation as a result of microbial and thermal processes (adapted from Hennessy and Knauth after Claypool and Kaplan, 1974). The actual depths and thicknesses of each reaction interval varies from site to site (Pisciotta and Mahoney, 1981; Lawrence, 1991).



of each reaction interval may vary from one location to the next (Lawrence, 1991).

The CO₂ generated in most of these reaction intervals carries a negative δ¹³C signature. However, microbial methanogenesis produces CO₂ that can be strongly enriched in ¹³C relative to PDB (Fig. 21). Methanogenic bacteria reduce organic matter (abbreviated as CH₂O) to carbon dioxide and methane by the following reaction:



(Irwin et al., 1977). The carbon dioxide produced by this reaction is strongly enriched in ¹³C relative to the methane (by 68.3‰ at 25°C; Bottinga, 1969).

Methanogenesis continues to produce ¹³C-enriched CO₂ until either (1) all the local organic material is consumed or (2) burial temperatures become too high to sustain the methanogenic bacteria (Hesse, 1986).

As temperatures increase during increased compaction, thermocatalytic decarboxylation of fatty acids begins to produce CO₂ (Fig. 21) by the following general reaction:



(Pisciotta and Mahoney, 1981). The CO₂ that is introduced to the system by decarboxylation is ¹³C-depleted and may cause a trend toward lower δ¹³C in authigenic carbonates (Irwin et al., 1977). Decarboxylation and methanogenesis can both be operative within the same depth interval (Pisciotta and Mahoney, 1981; Lawrence, 1991). However, as depth and temperature increase, the amount of CO₂ produced by methanogenic bacteria diminishes, and the CO₂

produced by decarboxylation reactions becomes more volumetrically significant (and thus more important for controlling the isotopic composition of Σ_{CO_2} ; Irwin et al., 1977).

The $\delta^{13}\text{C}$ values of the Prairie Canyon dolomites decrease from +10.7 to -9.7‰ (Fig. 6). Based on Figure 21, the strongly positive $\delta^{13}\text{C}$ values are indicative of carbonate that was enriched in ^{13}C as a result of preferential sequestering of ^{12}C by methane (Claypool and Kaplan, 1974) in the zone of methanogenesis. The negative $\delta^{13}\text{C}$ values, on the other hand, could have resulted from microbial oxidation or sulfate reduction reactions (i.e., before methanogenesis) or from thermocatalytic decarboxylation reactions (i.e., after methanogenesis). This ambiguity can be resolved if the isotopic data can be placed into a temporal framework.

Temporal relationship of isotopic data

In each of the cemented zones, $\delta^{18}\text{O}$ and $\delta^{13}\text{C}$ values are heaviest at the centers and decrease toward the edges. This suggests that the isotopically heavy dolomites precipitated first, and progressively lighter cements were added to the heavy core zones in concentric fashion. With this model, the isotopically lightest cements, which occur at the edges of the cemented zones, would have precipitated last. This temporal relationship helps to resolve the problem of whether the light $\delta^{13}\text{C}$ values at the edges of the cemented zones are a product of precipitation in the sulfate reduction zone or the zone of thermocatalytic decarboxylation. Because the ^{13}C -depleted dolomite precipitated after the ^{13}C -

enriched (methanic) cement, the light $\delta^{13}\text{C}$ values may be indicative of precipitation in the decarboxylation zone (Fig. 21).

A temporal trend from heavy to light $\delta^{13}\text{C}$ values may be correlated with the calculated oxygen isotope temperatures if it can be demonstrated that the pore-water $\delta^{18}\text{O}$ was not altered (i.e., by intrusion of meteoric water or by closed system precipitation of isotopically heavy authigenic minerals; see below) during progressive burial. The heaviest $\delta^{18}\text{O}$ values may reflect the lowest temperatures of precipitation (i.e., shallowest burial depths), and the trend toward lighter values may indicate an increase in temperature associated with greater compaction at depth. This explanation is consistent with late precipitation in the zone of thermocatalytic decarboxylation because the lightest $\delta^{13}\text{C}$ values are associated with the highest $\delta^{18}\text{O}$ temperatures (up to 84°C). As indicated in a previous section, this may reflect burial depths of up to 2.6 km. Such depths are not compatible with sulfate reduction because sulfate reduction typically occurs at low temperatures within several meters below the sediment-water interface (Pisciotta and Mahoney, 1981).

In summary, there is a temporal trend from (early) high $\delta^{13}\text{C}$ and $\delta^{18}\text{O}$ values to (late) low $\delta^{13}\text{C}$ and $\delta^{18}\text{O}$ values (Fig. 6). Because the positive (methanic) $\delta^{13}\text{C}$ values are associated with the lowest temperatures/depths, carbonate precipitation began during methanogenesis. With increasing time, compaction, and temperature, thermocatalytic decarboxylation became increasingly more important, and methanogenesis waned. This transition resulted in the change from heavy to light $\delta^{13}\text{C}$, and the increased temperature

resulted in the change from heavy to light $\delta^{18}\text{O}$ values. If this is the case, the linear trend in Figure 6 could correspond to the trend labeled “Prairie Canyon Dolomites” in Figure 21.

Evaluation of alternative hypotheses

Although it seems clear that the $\delta^{13}\text{C}$ values represent a temporal trend from methanic to decarboxylation signatures (Fig. 21), several fractionation mechanisms must be evaluated and/or eliminated to justify the $\delta^{18}\text{O}$ interpretations proposed thus far. For example, in order to make meaningful temperature calculations, the pore-water $\delta^{18}\text{O}$ has to be assumed to have been constant with depth. However, if pore-water $\delta^{18}\text{O}$ was lowered as a result of either (1) input of isotopically lighter meteoric water, or (2) Rayleigh-type precipitation of isotopically heavy authigenic material, the calculated dolomite $\delta^{18}\text{O}$ temperatures would be too high. Yet another process that could have resulted in depleted dolomite $\delta^{18}\text{O}$ values (and associated higher temperatures) is late-stage (deeper, higher temperature) recrystallization and re-equilibration of early, poorly ordered dolomite to a more stoichiometric phase. Each of these possibilities is evaluated in the sections below.

While evaluating these possibilities, it is important to keep in mind that the ideal interpretation must be consistent with the strong coupled decrease in $\delta^{13}\text{C}$ and $\delta^{18}\text{O}$ (Fig. 6) from the centers to the edges of the cemented zones (Figs. 7-16). It must also allow the earliest cements (in the centers of the

cemented zones) to have formed in the methanic zone, based on their heavy (positive) $\delta^{13}\text{C}$ values (Fig. 21). Further, the interpretation must account for the high minus-cement porosities, which are typically used as evidence for early (pre-compaction) precipitation. If precipitation did not initiate until the sediments had been buried (and compacted) into the methanic zone, why are the minus-cement porosities so high?

Intrusion of meteoric water (mixing of two end-member fluids)

One of the most widespread explanations in the literature for ^{18}O -depleted values in diagenetic carbonates is mixing with meteoric waters (e.g., Sass and Kolodny, 1972; Hudson, 1978; Carpenter, et al., 1988; Machemer and Hutcheon, 1988; Thyne and Boles, 1989; Bloch, 1990; Scotchman, 1991). Meteoric water has negative $\delta^{18}\text{O}$ values with respect to seawater (SMOW). If meteoric water intrudes through the subsurface into offshore areas, it may interact with sediment pore-waters early in the burial history of marine sediments and lower the $\delta^{18}\text{O}$ of the pore-water. As a result, authigenic minerals precipitated from the mixture of these two fluids should have more depleted oxygen isotope signatures than if they had been precipitated entirely from unaltered marine pore-waters.

This explanation can be invoked to account for the high minus-cement porosities because it allows for early (pre-compaction) precipitation of the cement. However, it does not explain the fractionation pattern of these samples, because an intrusion of meteoric water would have affected $\delta^{18}\text{O}$ more than $\delta^{13}\text{C}$. Although an influx of meteoric water would include some dissolved CO_2 , the

amount of carbon entering the system via the intrusion of meteoric water would be insignificant compared to the amount of carbon available locally from the decomposition of organic detritus. Furthermore, the amount of meteoric water that could have intruded into the offshore sediments of the Prairie Canyon Member would have been a function of the distance from the source of the meteoric water (i.e., onshore) to the zone of mixing. Because the four parasequences of the Middle Interval of the Prairie Canyon Member represent regressive-transgressive cycles (Cole and Young, 1991; Cole et al., submitted), the distance from shore to the site of precipitation had to have changed as sea level fluctuated. Therefore, the amount of meteoric water that could have reached the site of precipitation would have varied in response to changes in sea level. If this were the case, there would be a more cyclic fluctuation in $\delta^{18}\text{O}$ rather than the smooth linear decrease that is observed.

Precipitation of ^{18}O -enriched authigenic minerals

Some pore-water profiles in modern marine sediments show a decrease in $\delta^{18}\text{O}$ with depth that is unrelated to mixing with meteoric water (see references below). During low temperature diagenetic mineral precipitation, ^{18}O is preferentially fractionated into the solid phase. Therefore, precipitation of volumetrically significant quantities of authigenic minerals could result in a lowering of $\delta^{18}\text{O}$ in sediment pore-waters. This effect would be most dramatic in a closed system where precipitation of authigenic material could be modeled as a Rayleigh-type process. With no outside recharge of ^{18}O , pore-waters would

become progressively depleted in ^{18}O with time, and this depletion would be reflected in the $\delta^{18}\text{O}$ of the minerals precipitated from it. This has been shown to occur when authigenic clay minerals precipitate during diagenetic alteration of volcanogenic detritus (Lawrence et al., 1979; Lawrence and Gieskes, 1981; Lawrence and Tavianni, 1988). Although the Prairie Canyon sediments contain neither enough volcanogenic material nor enough authigenic clay to substantiate such an interpretation, they do contain volumetrically significant quantities of authigenic dolomite. Early (pre-compaction) precipitation of these cements could have resulted in ^{18}O -depleted pore-waters at shallow burial depths, and could explain the high minus-cement porosities of the cemented zones. In addition, the process could explain the observed temporal trend from heavy to light $\delta^{18}\text{O}$ values between the centers (early) and edges (late) of the Prairie Canyon dolomites. Mozley and Burns (1993) used a simple mass-balance calculation to show that if a sediment of original 70% porosity was reduced to 60% porosity by calcite precipitation in a closed system at 10°C , the $\delta^{18}\text{O}$ of the pore-water would decrease by 7.2‰. This suggests that if the Prairie Canyon dolomites had formed under similar conditions, isotopically heavy dolomites would have been precipitated before the lighter dolomites. This is because the late-stage (light $\delta^{18}\text{O}$) dolomite would have formed in equilibrium with isotopically lighter (with respect to $\delta^{18}\text{O}$) pore-water than had the heavy dolomites.

Unfortunately, this hypothesis does not offer an explanation for the coupled decrease in $\delta^{13}\text{C}$. As previously indicated, the strong linear correlation between $\delta^{13}\text{C}$ and $\delta^{18}\text{O}$ (Fig. 6) suggests that the fractionation mechanism that

affected oxygen also affected carbon simultaneously. If the 'system' is defined as the sediment pore-waters, such that the 'system' was closed with respect to input of *both* carbon and oxygen, then it is possible to envision a coupled decrease in the $\delta^{13}\text{C}$ of the dolomite as it consumed the available pore-water bicarbonate (i.e., in Rayleigh fashion). However, this would imply that the cements were precipitated from the Ca^{2+} , Mg^{2+} , and HCO_3^- contained in a single pore-volume of fluid. This is clearly not the case, as it would be impossible to precipitate volumes of dolomite in excess of 80% without importing some or all of these constituents from the surrounding sediments, their pore-waters, or overlying seawater. Furthermore, the high $\delta^{13}\text{C}$ values (up to 10.7‰ PDB) that occur in the centers of the cemented zones are indicative of CO_2 that was produced during microbial decomposition of organic material in the methanic zone. This isotopic evidence indicates that the 'system' (pore-water) was not closed with respect to carbon. Instead, there was a large reservoir present in the organic material that provided carbon to the pore-water as dissolved bicarbonate.

What if the 'system' was open with respect to carbon, but remained closed with respect to oxygen? Under these circumstances, the bicarbonate in the 'system;' would be rapidly depleted of ^{18}O during authigenic mineral precipitation while the bicarbonate $\delta^{13}\text{C}$ remained relatively unchanged. Thermocatalytic decarboxylation of organic matter would still have to be called upon to explain the ^{13}C -depleted values at the edges of the cemented zones.

Such an isotopic trend (rapidly depleted ^{18}O but slowly depleted ^{13}C) is not consistent with the smooth linear pattern shown in Figure 6.

Late-stage recrystallization of early cement

It is possible that early disordered dolomite (e.g., protodolomite) may have experienced isotopic re-equilibration at higher temperatures during a late-stage recrystallization event. If this were the case, the $\delta^{18}\text{O}$ temperatures (24-84°C) may represent the temperatures of the protodolomite-dolomite transition rather than the temperatures of primary precipitation. Therefore, a recrystallization scenario is consistent with the high minus-cement porosity of the cemented zones, because it allows for precipitation of large volumes of dolomite early in the diagenetic history of the sediments (Fig. 5 and Table 3). Furthermore, there are two chemically distinct generations of dolomite that are visible in BSE images (Figs. 19a, 19b). Dark (low-Fe) dolomite precipitated earlier than the more ferroan (and much more volumetrically significant) light-colored dolomite. The BSE images reveal that some of the dark dolomite crystals have irregular outlines. These features could have resulted from a recrystallization event.

There are several problems with this hypothesis. Although some of the dark (early, Fe-poor) dolomite has irregular crystal boundaries which could support recrystallization, there is no simple two-phase mixing apparent in the BSE images. If (1) the light (ferroan) dolomite was recrystallized from the earlier, dark dolomite, and (2) the two phases are isotopically distinct, then there

would have to be an increase in the light-to-dark ratio from core to edge to explain the $\delta^{18}\text{O}$ decrease across that interval. However, point-counts of 11 digital BSE photomicrographs indicate that the ratio remains constant throughout the cemented zones. The photomicrographs are from various sample points (centers, edges, and points in between) within Grids 10 (Sequence D; concretion), 11 (Sequence D; continuous) and 18 (Sequence A; continuous). The light-to-dark ratio in *all* of these photomicrographs is approximately 5:1 which suggests that the isotopic variation did not result from simple mixing of different proportions of the light and dark phases.

Although a recrystallization hypothesis could be used to explain the ^{18}O -depleted signatures at the edges of the cemented zones, it fails to explain the coupled decrease in $\delta^{13}\text{C}$. The $\delta^{18}\text{O}$ of dolomite crystals that have experienced recrystallization would have been affected by (1) the ambient temperature at the time of recrystallization; and (2) the $\delta^{18}\text{O}$ of the pore-fluid. However, the $\delta^{13}\text{C}$ would have remained largely unchanged after recrystallization (Morad and Eshete, 1990) because carbon isotopes are not as responsive to temperature-related fractionation as oxygen isotopes (Veizer, 1983; Gautier and Claypool, 1984). Moreover, large volumes of pre-existing dolomite cement would have acted as a virtually unlimited reservoir for carbon compared to the relatively small amount of carbon dissolved in the sediment pore-waters. Therefore, recrystallization at higher temperatures would have affected the $\delta^{18}\text{O}$ of the cement to a much greater extent than its $\delta^{13}\text{C}$, and is not compatible with the covariance between both isotopes.

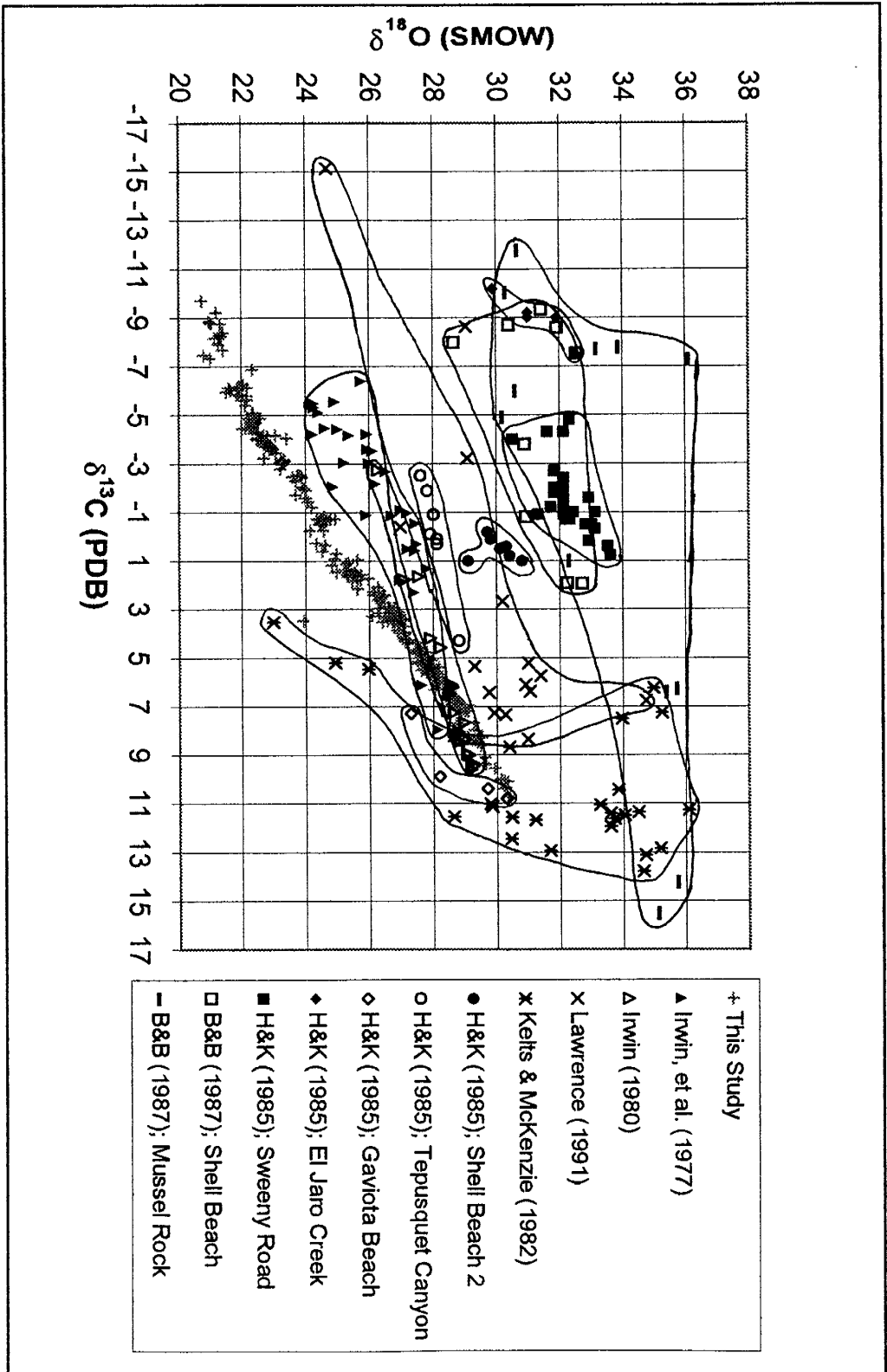
Comparison with data from other studies

Simultaneous decreases in $\delta^{13}\text{C}$ and $\delta^{18}\text{O}$ have been documented by other investigators of marine dolomites (see references below). The results of eleven stable isotopic data sets from six previous studies have been compiled for comparison with the results of this study (Fig. 22). All of the data sets in this compilation are from organic-rich, marine sediments, and have positive $\delta^{13}\text{C} - \delta^{18}\text{O}$ slopes (although some of the data sets have more scatter than others). Data sets were omitted if they did not have (1) a positive $\delta^{13}\text{C} - \delta^{18}\text{O}$ slope, and (2) at least four data points. Only samples that were confirmed to be dolomite, Fe-dolomite, or ankerite by microprobe and/or petrographic analyses were plotted. The data sets that met these criteria include two sets from the Upper Jurassic Kimmeridge Clay (Irwin, et al., 1977; Irwin, 1980), seven from the Miocene Monterey Formation (five from Hennessy and Knauth, 1985; two from Burns and Baker, 1987), one from the Late Cretaceous Herring Formation (Lawrence, 1991), and one from the modern Guaymas Slope (Hole 479; Kelts and McKenzie, 1982). Oxygen isotope values reported relative to PDB were converted to the SMOW scale via the relationship:

$$\delta^{18}\text{O}_{\text{SMOW}} = 1.03 * \delta^{18}\text{O}_{\text{PDB}} + 30.86\text{‰}$$

(Hoefs, 1987). One dolomite sample from Lawrence (1991) was omitted from this compilation because it had an extremely light $\delta^{13}\text{C}$ value (-36.67‰ , PDB) and did not plot anywhere near the rest of the dolomites, which are in the range $-17\text{‰} < \delta^{13}\text{C} < +17\text{‰}$, PDB (Fig. 22).

Figure 22: Compilation of marine dolomite isotopic compositions Abbreviations: H&K = Hennessy and Knauth; B&B = Burns and Baker.



Simultaneous decreases in both $\delta^{13}\text{C}$ and $\delta^{18}\text{O}$ are apparently a common occurrence for marine dolomite cements in organic-rich sediments (Fig. 22). In most of these studies, the authors have interpreted the systematic isotopic covariation to reflect dolomite growth during progressive burial, as is suggested for the Prairie Canyon dolomites. Lawrence (1991) and Burns and Baker (1987) acknowledged this interpretation guardedly, however, because of evidence that the $\delta^{18}\text{O}$ of dolomites in the Herring and Monterey Formations, respectively, had been modified during recrystallization and dolomitization of precursor calcite. It is possible that the large amount of scatter associated with these authors' data (Fig. 22) is an artifact of such a recrystallization event.

In general, however, the overall positive slopes of the various data sets suggest that the diagenetic processes responsible for dolomite precipitation in the Prairie Canyon Member may be widespread. For example, most of the isotopic trends begin with methanic (positive $\delta^{13}\text{C}$) values and end with inferred decarboxylation signatures (negative $\delta^{13}\text{C}$ and higher oxygen isotope temperatures). This suggests that deep (i.e., depths of several hundred meters to several kilometers) precipitation of authigenic dolomite may be more common than shallow precipitation in spite of textural evidence (i.e., high minus-cement porosity) that suggests shallow precipitation.

There are several similarities between the two Kimmeridge Clay data sets (Irwin et al., 1977; Irwin, 1980) and the Prairie Canyon dolomites. Each of these data sets spans a similar range of isotopic compositions (Fig. 22) and includes $\delta^{13}\text{C}$ signatures that reflect their origins in the zones of methanogenesis and

thermal decarboxylation. In addition, both the Kimmeridge and Prairie Canyon data sets have more scatter among the data at the isotopically light (decarboxylation) ends of their respective linear trends. This may be the result of differential availability of suitable molecules for decarboxylation reactions after much of the organic matter and fatty acids had been consumed by earlier microbial and/or thermal processes. In any case, the geochemical similarity between the Kimmeridge and Prairie Canyon dolomites suggests that the two resulted from very similar geologic and diagenetic environments.

Explanation of high minus-cement porosities

Given that $\delta^{18}\text{O}$ modification via meteoric water intrusion, closed system precipitation, or recrystallization scenarios can be ruled out, it seems the most likely explanation for the coupled isotopic fractionation (Fig. 6) is that both the oxygen and carbon isotopic compositions are related to burial depth (see previous section, "*Temporal relationship of isotopic data*"). Although this hypothesis is adequate to explain the linear relationship between $\delta^{18}\text{O}$ and $\delta^{13}\text{C}$ (Fig. 6), another process needs to be invoked to explain the high minus-cement porosities (> 80%) that are observed in thin section. As previously noted, high minus-cement porosities are typically used as evidence for early (pre-compaction) cementation, rather than of cementation that initiated at depths of several hundreds of meters. This paradox can be explained if a small amount of early cementation had occurred that was not enough to fill the existing pore-space, but that was enough to stabilize the sediments during subsequent

compaction. If this were the case, these zones could have become preferential pathways for fluid after compaction had reduced the porosity of the surrounding sediments. The upward expulsion of fluids into the cemented zones may have even resulted in local fluid overpressure that could have helped these zones to resist compaction, even at substantial depths. This scenario could account for the high minus-cement porosities, because it allows for emplacement of late-stage cements throughout the interiors of the cemented zones. Further, such a scenario is supported by recent studies that show that marine carbonate concretions commonly contain significant late-stage cements within their interiors (Jordan et al., 1992; Mozley, 1996). It also solves the puzzle of how dense cemented layers and concretions in the Prairie Canyon Member could have been supported by low density, high porosity mud, without foundering due to the density contrast (i.e., much of the cementation could have occurred after the density contrast was diminished due to compaction; see discussion in Mozley, 1996).

As previously indicated, two stages of cementation were documented in BSE images of the Prairie Canyon dolomites. The early, Fe-poor dolomite makes up approximately 17% of the total volume of cement. This early phase may have precipitated at shallow burial depths, and its presence may have been sufficient to hold the pore-space open during subsequent compaction. There is approximately five times more late-stage, ferroan cement than early, Fe-poor cement (5:1 ratio) so the whole-rock isotopic composition at any position in the

cemented zones may be controlled by that of the ferroan (more volumetrically significant) cement.

Kantorowicz et al. (1987) suggested that early cementation could occur during periods of extremely low sedimentation rate in the microbial oxidation zone (i.e., at, or immediately below, the sediment-water interface; Fig. 21), and that such cements may be isotopically homogeneous (see Fig. 11 of Kantorowicz et al., 1987). Most of the Prairie Canyon cements occur at the tops of coarsening-upward parasequences (Cole and Young, 1991), and abrupt deepening at the parasequence tops could have caused a decrease in sedimentation rate and an associated increase in the amount of time that the uppermost sediments were resident in the microbial oxidation zone (see discussion in Taylor et al., 1995). The increased residence time in the oxic zone may have permitted precipitation of the early, Fe-poor (dark) cement. Iron in this zone is typically present in its +3 oxidization state, and Fe^{3+} is not readily incorporated into the dolomite crystal lattice. Further, if the Fe-poor dolomite is indeed isotopically homogeneous, then this hypothesis is compatible with the later, more volumetrically significant, ferroan dolomite being responsible for the isotopic variability of the Prairie Canyon dolomites. However, spot ion microprobe isotopic analyses would be necessary to test this idea.

Spatial distribution of C and O isotopes

Mesoscopic (outcrop scale) isotopic zonation

As suggested by the core to edge relationships and the oxygen isotope temperatures, precipitation of the isotopically heavy dolomites preceded that of the lighter dolomites. However, several questions remain unanswered about the spatial distribution of C and O isotopes at the outcrop scale. For example, what mode of growth was responsible for the formation of the concretions and laterally continuous horizons? Why are the isotopically heavy core zones of the continuously cemented horizons situated below the geometric centers of the layers? Are the spatial isotopic signatures of the concretions distinguishable from those of the laterally extensive horizons? These questions will be addressed in this section.

The growth model of Bjørkum and Walderhaug (1990) suggests that laterally extensive horizons result from coalescence of stratabound concretions, and is consistent with the temporal and spatial distribution of C and O isotopes in the Prairie Canyon cements (Figs. 7-16). The Prairie Canyon concretions and laterally extensive horizons have considerably more vertical isotopic variation (in both $\delta^{13}\text{C}$ and $\delta^{18}\text{O}$) than horizontal variation. However, horizontal isotopic variation is greater in the isotopically heavy cores (centers) of the cemented zones (both concretionary and laterally extensive) than at the edges: compare Figures 7 and 13. Figure 7 (Grid 9) is a laterally continuous horizon, and Figure 13 (Grid 10) is the right half of a concretion (the left side of the grid bisects the physical center of the concretion). The Grid 10 concretion (Fig. 13) has a

concentric zonation about the isotopically heavy core of the concretion which exhibits closure about the right side of the grid. The geometry of this isotopic zonation closely approximates the physical shape of the concretion and is very similar to the geometry of the two isotopically heavy zones in the core of Grid 9 (Fig. 7). The isotopic pattern in Grid 9 (Fig. 7) may be a record of the merger of two concretions (one bisected by the left side of the grid and the other just right of center) that were originally similar to the Grid 10 (Fig. 13) concretion. After the concretions merged, continued precipitation resulted in growth above and below the merged concretions. However, more growth occurred above (i.e., in the 'up' direction) than below the concretions. This is evidenced by the occurrence of the lightest (i.e., latest stage) $\delta^{13}\text{C}$ and $\delta^{18}\text{O}$ values at the tops of both of the continuous layers (Sequence D: Figs. 7-9; Sequence A: Figs. 10-12) and by the presence of more cement above the core zones than below (i.e., the core zones are situated below the geometric centers of the layers). This observation contrasts with that of Irwin (1980), who found that the last stages of cementation occurred on the underside of the Yellow Ledge, a laterally continuous dolomite horizon in the Kimmeridge Clay Formation.

Similar patterns can be seen elsewhere in the same cemented layer (continuous layer near top of Sequence D; Fig. 4). Grids 11 and 13 (Figs. 8 and 9, respectively) have isotopically heavy zones in their centers that may be the cross-sections of early stratabound concretions prior to coalescence. After concretions merged and the layer became continuous, growth continued above and below the early core zones (with more growth above than below) as it had at

Grid 9. The continuous layer at the base of Sequence A (Grids 15, 16, and 18; Figs. 10, 11, and 12) may also be the result of the coalescence of concretions, but that is difficult to evaluate because of the lower horizontal sampling density in those grids.

Although the isotopically heavy core zones of the laterally continuous horizons are located below the physical centers of the horizons, the same is not true of the concretions. For the concretions, the heavy core zones are situated in the geometric centers of the concretions. This suggests that the two types of cemented zones may be distinguishable from one another by their spatial isotopic distributions.

Macro- and megascopic (regional scale) isotopic patterns: implications for geochemical correlation

Each of the cemented layers (concretionary or continuous) that were sampled at multiple locations has an isotopic signature that is persistent over large lateral distances. Three layers were sampled at multiple locations: one from Sequence A (continuous) and two from Sequence D (one continuous and one concretionary). Each of these layers has a characteristic range and spatial distribution of $\delta^{13}\text{C}$ and $\delta^{18}\text{O}$ that recorded the timing and conditions of dolomite precipitation.

Table 5 is a summary of the ranges of $\delta^{13}\text{C}$ and $\delta^{18}\text{O}$ values for each grid in Sequence A (continuous) and Sequence D (concretionary and continuous). Shown also is the mean maximum and mean minimum values for each layer and

Table 5: Summary of maximum and minimum $\delta^{13}\text{C}$ and $\delta^{18}\text{O}$ values for each grid in the three layers that were sampled at multiple locations. Each layer has a diagnostic range of $\delta^{13}\text{C}$ and $\delta^{18}\text{O}$ that could be used to geochemically correlate the layer in the subsurface (see text). $\delta^{13}\text{C}$ values are reported relative to PDB, and $\delta^{18}\text{O}$ values are relative to SMOW.

Sequence	Type	Grid	Area	Figure	max $\delta^{18}\text{O}$	min $\delta^{18}\text{O}$	max $\delta^{13}\text{C}$	min $\delta^{13}\text{C}$
D	concretions	10	2	13	30.4	22.6	10.7	-4.9
		12	4	14	30.4	24.5	10.7	-0.8
mean for layer \pm maximum difference					30.4 ± 0.0	23.6 ± 1.0	10.7 ± 0.0	-2.9 ± 2.1
D	continuous	9	2	7	29.0	20.7	7.2	-9.7
		11	4	8	29.1	21.8	7.3	-6.1
		13	4	9	28.8	21.0	7.0	-8.8
mean for layer \pm maximum difference					29.0 ± 0.2	21.2 ± 0.6	7.2 ± 0.2	-8.2 ± 2.1
A	continuous	15	2	10	28.0	23.1	5.5	-4.1
		16	2	11	28.1	22.9	5.7	-3.8
		18	3	12	27.8	22.7	5.5	-3.2
mean for layer \pm maximum difference					28.0 ± 0.2	22.9 ± 0.2	5.6 ± 0.1	-3.7 ± 0.5

the maximum difference (\pm) from those means. Where the difference (\pm) is negligible (i.e., less than 0.5‰), the range between these maximum and minimum mean values can be used as an isotopic fingerprint for each layer that could presumably be used to geochemically correlate it throughout the Prairie Canyon area. Larger differences (\pm) are associated with lesser correlation confidence. In general, all the maximum (core) mean values for both $\delta^{13}\text{C}$ and $\delta^{18}\text{O}$ have a small difference from their mean for the layer ($\pm 0.2\%$ or less), and the minimum (edge) mean values have larger differences (up to $\pm 2.1\%$). The larger differences (\pm) at the edges may be an artifact of differential erosion and weathering from site to site. The upper edges of some of the outcrops are weathered, and in some cases, large chunks of the edges have been removed by erosion and could not be sampled (resulting in odd-shaped grids such as Grids 12, 17, and 18). Presumably, this would not be a problem in less weathered samples (i.e., subsurface core material).

The fact that diagnostic isotopic patterns persist over large lateral intervals at the surface has important implications for geochemical correlation of low-permeability cemented zones in the subsurface. Although concretions may only affect fluid flow locally, continuously cemented layers such as the two in this study can restrict, or even eliminate, vertical fluid movement (Kantorowicz et al., 1987). Cemented zones are commonly encountered during subsurface drilling operations. However, because the well-bore only provides a vertical section through these zones, their lateral dimensions cannot be readily established. Therefore, the ability to correlate these low-permeability zones between adjacent

wells could aid in establishing the geometry of the reservoir and promote effective reservoir exploitation. Because the isotopic variation in the Prairie Canyon samples is dominantly in the vertical direction, it may be possible to make a positive identification of any layer from a vertical core section in spite of the limited dimensions of the well-bore. Furthermore, because the concretions and laterally continuous horizons have different spatial (particularly vertical) isotopic distributions, it may be possible to distinguish between the two types of cementation by analysis of isotopic data from subsurface core material.

Geochemical correlation may not be possible in every circumstance. Although unlikely, it is not impossible that two layers could have identical geochemical properties and thus be undifferentiable, especially in structurally complex areas where relative stratigraphic positions are more difficult to ascertain. It is also possible that a concretion could be mistaken for a continuously cemented horizon, or vice-versa. Finally, there is no guarantee that every carbonate-cemented horizon has a laterally persistent geochemical signature; the Prairie Canyon dolomites may be the exception rather than the norm. Walderhaug et al. (1989) concluded that geochemical analysis may only be of limited value for correlation of the calcite cemented layers of the Fensfjord Formation in the Brage Field. Their conclusion is based on significantly different isotopic and trace element signatures between two vertical sampling traverses spaced 30 cm laterally apart in the same layer.

CONCLUSIONS

- (1) Detailed small-scale sampling is required to adequately characterize the spatial distribution of carbon and oxygen isotopes in carbonate cements at the outcrop (mesoscopic) scale. Small-scale data sets must be nested within the larger regional (macro- to megascopic) and stratigraphic framework in order to reliably correlate cements from one location to the next.
- (2) $\delta^{13}\text{C}_{\text{dol}}$ values indicate that the Prairie Canyon dolomites incorporated CO_2 that was generated during organic matter decomposition. Strongly positive $\delta^{13}\text{C}_{\text{dol}}$ values suggest ^{13}C -enrichment during methanogenesis, and ^{13}C -depleted dolomites may reflect later (deeper, higher temperature) precipitation during thermocatalytic decarboxylation. This is consistent with a trend from low to high oxygen isotope temperatures, and with core to edge decreases in both $\delta^{13}\text{C}$ and $\delta^{18}\text{O}$.
- (3) The Prairie Canyon dolomites show a strong linear relationship ($R^2=0.984$) between $\delta^{13}\text{C}$ and $\delta^{18}\text{O}$ that suggests that both isotopes were fractionated by a common process. Isotopic covariance is not uncommon in the literature, and most authors interpret the transition from heavy to light $\delta^{13}\text{C}$ and $\delta^{18}\text{O}$ values as indicative of dolomite precipitation during progressive burial.

- (4) Each cemented layer (concretionary or continuous) in the Middle Interval of the Prairie Canyon Member has a characteristic spatial isotopic distribution that is persistent over lateral intervals of up to 1.5 km (and possibly more). This suggests that it may be possible to geochemically correlate these horizons in the subsurface.
- (5) It may be possible to distinguish concretionary cements from laterally continuous cements based on differences in their spatial isotopic distributions. The Prairie Canyon concretions have isotopically heavy core zones that occur in their physical centers. The continuous horizons also have heavy core zones, but they are situated below the physical centers of the continuous layers (i.e., there is more cement above the core zones than below). These observations suggest that continuous horizons resulted from lateral coalescence of stratabound concretions. Growth continued above and below the laterally extensive layers, but most of the growth occurred above the merged concretions (i.e., in the 'up' direction).

REFERENCES CITED

- Alpay, O.A., 1972, A practical approach to defining reservoir heterogeneity: *Journal of Petroleum Technology*, v. 24, p. 841-848.
- Baker, P.A. and Burns, S.J., 1985, The occurrence and formation of dolomite in organic-rich continental margin sediments: *Am. Assoc. Petroleum Geologists Bull.*, v. 69, p. 1917-1930.
- Bjørkum, P.A. and Walderhaug, O., 1990b, Lateral extent of calcite-cemented zones in shallow marine sandstones: *in* North Sea oil and gas reservoirs-II: The Norwegian Institute of Technology (Graham & Trotman), p. 331-336.
- Bjørkum, P.A. and Walderhaug, O., 1993, Isotopic composition of a calcite-cemented layer in the Lower Jurassic Bridport Sands, southern England: Implications for formation of laterally extensive calcite-cemented layers: *Journal of Sedimentary Petrology*, v. 63, no. 4, p.678-682.
- Bloch, J., 1990, Stable isotopic composition of authigenic carbonates from the Albian Harmon Member (Peace River Formation): evidence of early diagenetic processes: *Bulletin of Canadian Petroleum Geology*, v. 38, p. 39-52.
- Bottinga, Y., 1969, Calculated fractionation factors for carbon and hydrogen isotope exchange in the system calcite-carbon dioxide-graphite-methane-hydrogen-water vapor: *Geochimica et Cosmochimica Acta*, v. 33, p. 49-64.
- Carpenter, S.J., Erickson, J.M., Lohmann, K.C., and Owen, M.R., 1988, Diagenesis of fossiliferous concretions from the Upper Cretaceous Fox Hills Formation, North Dakota: *Journal of Sedimentary Petrology*, v. 58, p. 706-723.
- Claypool, G.E. and Kaplan, I.R., 1974, The origin and distribution of methane in marine sediments: *in* Kaplan, I.R., ed., *Natural Gases in Marine Sediments*: New York, Plenum Press, p. 99-140.
- Cole, R.D. and Young, R.G., 1991, Facies characterization and architecture of a muddy shelf-sandstone complex: "Mancos B" interval of Upper Cretaceous Mancos Shale, Northwest Colorado-Northeast Utah: *in* Miall, A.D., and Tyler, Noel, eds., *The three-dimensional facies architecture of terrigenous clastic sediments and its implications for hydrocarbon discovery and recovery*: Society of Economic Paleontologists and Mineralogists, *Concepts in Sedimentology and Paleontology*, v. 3, p. 277-287.

Cole, R.D., Young, R.G., and Willis, G.C., submitted, The Prairie Canyon Member, a new unit of the Upper Cretaceous Mancos Shale, west-central Colorado and eastern Utah, submitted.

Fouch, T.D. and Cashion, W.B., 1979, Distribution of rock types, lithologic groups, and interpreted depositional environments for some Lower Tertiary and Upper Cretaceous rocks from outcrops at Willow Creek-Indian Canyon through the subsurface of Duchesne and Altamony oil fields, southwest of north-central parts of the Uinta Basin, Utah: USGS Open-File Report 79-365, 2 sheets.

Fritz, P. and Smith, D.G.W., 1970, The isotopic composition of secondary dolomites: *Geochimica et Cosmochimica Acta*, v. 34, p. 1161-1173.

Gautier, D.L. and Claypool, G.E., 1984, Interpretation of methanic diagenesis in ancient sediments by analogy with processes in modern diagenetic environments: *in* Mc Donald, D.A. and Surdam, R.C., eds., *Clastic Diagenesis*, AAPG Mem., v. 37, p. 111-123.

Hennessy, J. and Knauth, L.P., 1985, Isotopic variations in dolomite concretions from the Monterey Formation, California: *Journal of Sedimentary Petrology*, v. 55, p. 120-130.

Hesse, R., 1986, Early diagenetic pore water/sediment interaction: modern offshore basins: *Geoscience Canada*, v. 13, no. 3, p. 165-196.

Hoefs, J., 1987, *Stable Isotope Geochemistry*, Springer-Verlag, Berlin, 241 pp.

Hudson, J.D., 1978, Concretions, isotopes, and the diagenetic history of the Oxford Clay (Jurassic) of central England: *Sedimentology*, v. 25, p. 339-370.

Irwin, H., 1980, Early diagenetic carbonate precipitation and pore fluid migration in the Kimmeridge Clay of Dorset, England: *Sedimentology*, v. 27, p. 577-591.

Irwin, H., Curtis, C.D., and Coleman, M., 1977, Isotopic evidence for source of diagenetic carbonates formed during burial of organic rich sediments: *Nature*, v. 269, p. 209-213.

Jordan, M.M., Curtis, C.D., Aplin, A.C., and Coleman, M.L., 1992, Access of pore waters to carbonate precipitation sites during concretion growth: *in* Kharaka and Maest, eds., *Water-Rock Interaction*: Rotterdam, Balkema, p. 1239-1242.

- Kantorowicz, J.D., Bryant, I.D., and Dawans, J.M., 1987, Controls on the geometry and distribution of carbonate cements in Jurassic sandstones: Bridport Sands, southern England and Viking Group, Troll Field, Norway, *in* Marshall, J.D., ed., *Diagenesis of sedimentary sequences*: Oxford, Blackwell, p. 103-118.
- Kellogg, H.E., 1977, Geology and petroleum of the Mancos B Formation, Douglas Creek Arch area, Colorado and Utah: *in* Veal, H.K., ed., *Exploration frontiers of the central and southern Rockies*: Rocky Mountain Association of Geologists, p. 108-110.
- Kelts, K.R. and McKenzie, J.A., 1982, Diagenetic dolomite formation in Quaternary anoxic diatomaceous muds of Deep Sea Drilling Project Leg 64, Gulf of California: Initial Reports of the Deep Sea Drilling Project, v. 64, p.553-569.
- Kopper, P.K., 1962, Douglas Creek anticline and adjoining area: *in* Amuedo, C.L., and Mott, M.R., eds., *Exploration for Oil and Gas in Northwestern Colorado*: Rocky Mountain Association of Geologists, p. 108-110.
- Land, L.S., 1983, The application of stable isotopes to studies of the origin of dolomite and to problems of diagenesis in clastic sediments: *in* *Stable Isotopes in Sedimentary Geology*, SEPM Short Course 10, 4.1-4.22.
- Lawrence, J.R. and Gieskes, J.M., 1981, Constraints on water transport and alteration in the oceanic crust from isotopic composition of pore water: *Journal of Geophysical Research*, v. 86, p. 7924-7934.
- Lawrence, J.R. and Taviani, M., 1988, Extreme hydrogen, oxygen, and carbon isotope anomalies in the pore waters and carbonates of the sediments and basalts from the Norwegian Sea: methane and hydrogen from the mantle?: *Geochimica et Cosmochimica Acta*, v. 52, p. 2077-2083.
- Lawrence, J.R., Drever, J.I., Anderson, T.F., and Brueckner, H.K., 1979, Importance of alteration of volcanic material in the sediments of Deep Sea Drilling site 323: chemistry, $^{18}\text{O}/^{16}\text{O}$, and $^{87}\text{Sr}/^{86}\text{Sr}$: *Geochimica et Cosmochimica Acta*, v. 43, p. 573-588.
- Lawrence, M.J.F., 1991, Early diagenetic dolomite concretions in the late Cretaceous Herring Formation, eastern Marlborough, New Zealand: *Sedimentary Geology*, v. 75, p. 125-140.
- Machemer, S.D. and Hutcheon, I., 1988, Geochemistry of early carbonate cements in the Cardium Formation, Central Alberta: *Journal of Sedimentary Petrology*, v. 58, p. 136-147.

- McCrea, J.M., 1950, On the isotopic chemistry of carbonates and a paleotemperature scale: *Journal of Chemical Physics*, v. 18, p. 849-857.
- Morad, S., Al-Aasm, I.S., Ramseyer, K., Marfil, R., and Aldahan, A.A., 1990, Diagenesis of carbonate cements in Permo-Triassic sandstones from the Iberian Range, Spain: evidence from chemical composition and stable isotopes: *Sedimentary Geology*, v. 67, p. 281-295.
- Morad, S. and Eshete, M., 1990, Petrology, chemistry, and diagenesis of calcite concretions in Silurian shales from central Sweden: *Sedimentary Geology*, v. 66, p. 113-134.
- Mozley, P.S. and Carothers, W.W., 1992, Elemental and isotopic composition of siderite in the Kuparuk Formation, Alaska: Effect of microbial activity and water/sediment interaction on early pore-water chemistry: *Journal of Sedimentary Petrology*, v. 62, no. 4, p. 681-692.
- Mozley, P.S. and Burns, S.J., 1993, Oxygen and carbon isotopic composition of marine carbonate concretions: an overview: *Journal of Sedimentary Petrology*, v. 63, no. 1, p. 73-83.
- Mozley, P.S., 1996, The internal structure of carbonate concretions in mudrocks: a critical evaluation of the conventional concentric model of concretion growth: *Sedimentary Geology*, v. 103, p. 85-91.
- Northrop, D.A. and Clayton, R.N., 1966, Oxygen isotope fractionations in systems containing dolomite: *Journal of Geology*, v. 74, p. 174-195.
- O'Neil, J.R. and Epstein, S., 1966, Oxygen isotope fractionation in the system dolomite-calcite-carbon dioxide: *Science*, v. 152, p. 198-201.
- Phillips, F.M., Campbell, A.R., Kruger, C., Johnson, P., Roberts, R., and Keyes, E., 1992: A reconstruction of the response of the water balance in western U.S. lake basins to climatic change: Technical Completion Report #269, Vol. 1 and 2; New Mexico Water Resources Research Institute, New Mexico State University.
- Pisciotta, K.A. and Mahoney, J.J., 1981, Isotopic survey of diagenetic carbonates, Deep Sea Drilling Project leg 63: *in* Initial Reports of the Deep Sea Drilling Project, v. 63, p. 595-609.
- Raiswell, R., 1976, The microbiological formation of carbonate concretions in the Upper Lias of NE England: *Chemical Geology*, v. 18, p. 227-244.

- Rosenbaum, J. and Sheppard, S.M.F., 1986, An isotopic study of siderites, dolomites, and ankerites at high temperatures: *Geochimica et Cosmochimica Acta*, v. 50, p. 1147-1150.
- Sass, E. and Kolodny, Y., 1972, Stable isotopes, chemistry, and petrology of carbonate concretions (Mishash Formation, Israel): *Chemical Geology*, v. 10, p. 261-286.
- Scotchman, I.C., 1991, The geochemistry of concretions from the Kimmeridge Clay Formation of southern and eastern England: *Sedimentology*, v. 38, p. 79-106.
- Shackleton, N.J. and Kennett, J.P., 1975, Late Cenozoic oxygen and carbon isotopic change at DSPD site 284: implications for the glacial history of the Northern Hemisphere, *in* Kennett, J.P., Houtz, R.E., et al., eds., Initial reports of the Deep Sea Drilling Project, v. 29: U.S. Government Printing Office, p. 801-807.
- Taylor, K.G., Gawthorpe, R.L., and Van Wagoner, J.C., 1995, Stratigraphic control on laterally persistent cementation, Book Cliffs, Utah: *Journal of the Geological Society, London*, v. 152, p. 225-228.
- Thyne, G.D. and Boles, J.R., 1989, Isotopic evidence for origin of the Moeraki septarian concretions, New Zealand: *Journal of Sedimentary Petrology*, v. 59, p. 272-279.
- Veizer, J., 1983, Trace elements and isotopes in sedimentary carbonates: *in* R.J. Reeder, ed., *Carbonates: Mineralogy and Chemistry*, Mineral. Soc. Am., *Rev. Mineral.*, v. 11, p. 265-299.
- Walderhaug, O., Bjørkum, P.A., and Nordgård Bolås, H.M., 1989, Correlation of calcite-cemented layers in shallow-marine sandstones of the Fensfjord Formation in the Brage Field: *in* Collinson, J.D., ed., *Correlation in Hydrocarbon Exploration*, Graham and Trotman, London, p. 367-375.
- Wilkinson, M., 1991, The concretions of the Bearreraig Sandstone Formation: geometry and geochemistry: *Sedimentology*, v. 38, p. 899-912.
- Wilkinson, M., 1992, Concretionary cements in Jurassic sandstones, Isle of Eigg, Inner Hebrides: *in* Parnell, J., ed., *Basins on the Atlantic Seaboard: Petroleum Geology, Sedimentology, and Basin Evolution*, Geological Society Special Publication No. 62, p. 145-154.

Wilkinson, M., 1993, Concretions of the Valtos Sandstone Formation of Skye: geochemical indicators of palaeo-hydrology: *Journal of the Geological Society, London*, v. 150, p. 57-66.

Young, R.G., 1955, Sedimentary facies and intertonguing in the Upper Cretaceous of the Book Cliffs, Utah-Colorado: *Geological Society of America Bulletin*, v. 66, p. 177-202.

Young, R.G., 1959, Cretaceous deposits of the Grand Junction area, Garfield, Mesa, and Delta counties, Colorado: *in* Haun, J.D., and Wiemer, R.J., eds., *Symposium on Cretaceous Rocks of Colorado and Adjacent Areas*: Rocky Mountain Association of Geologists, p. 17-25.

Young, R.G., 1960, Mancos Shale and Mesaverde Group of Palisades Area: *in* R.J. Weimer, and J.D. Haun, eds., *Guide to the Geology of Colorado*: Geological Society of America, Rocky Mountain Association of Geologists, and Colorado Scientific Society, p. 85-86.

APPENDIX 1:

Regional Structural Provinces

1. Uncompahgre Plateau

Rising above the south side of the Grand Valley is the Uncompahgre Plateau. At this location, Precambrian gneisses and schists (1.7 Ga) are unconformably overlain by Upper Triassic metasediments of the Chinle and Wingate Formations. The prominent cliffs of the eolian Wingate Sandstone are capped by the resistant, silica-cemented Kayenta Formation. The Upper Jurassic Entrada, Summerville, and Morrison Formations are located upsection from the Kayenta, and the Morrison is overlain with Cretaceous sediments of the Burro Canyon, Dakota, and Mancos Formations. The Colorado National Monument, near Grand Junction, is an excellent place to view the Mesozoic stratigraphy and Laramide structures of the Uncompahgre Plateau, but the Mancos Shale has been entirely eroded at the Monument.

The Uncompahgre Plateau has enjoyed at least four generations of structural deformation. The first generation occurred during the Ancestral Rockies orogeny (Pennsylvanian-Permian). Crustal shortening led to faulting and initial uplift of the plateau. Two periods of lesser uplift in the middle Triassic and middle Jurassic are marked by an absence of strata from those periods. Most of the elevation of the modern plateau is the result of uplift and deformation during the Laramide orogeny (late Cretaceous to late Paleocene). During this time, pre-existing, northwest-trending, high-angle (70°-85°) faults in the

Precambrian basement were reactivated. The result was monoclinal folding of the overlying Mesozoic sandstones (especially of the Wingate Formation) along shear fractures and microfaults. Sandstones overlying lower angle normal faults (less than 70°) were fractured and faulted rather than folded (Heyman, et al., 1986).

2. Douglas Creek Arch

The Douglas Creek Arch is a complex, north-trending structure which extends northward from near the Prairie Canyon type area to near Rangely, Colorado. The arch is characterized by a series of northwest-trending anticlines and a well-developed series of northeast-striking normal faults. In addition, a west-northwest-striking fault system, which roughly parallels the trend of the Uncompahgre uplift, underlies much of the arch. The Douglas Creek Arch separates two major Laramide structural and sedimentary basins, the Uinta Basin to the west, and the Piceance Creek Basin to the east (Johnson and Finn, 1986). The Prairie Canyon Member of the Mancos Shale is well-recognized in the subsurface along the arch where it is a major producer of natural gas and a minor producer of oil (Cole and Young, 1991).

Stone (1977) has shown that formation of the ancestral Douglas Creek Arch began at least as early as the Middle Triassic. This is evidenced by southward truncation of all formations below the Shinarump Conglomerate (Upper Triassic) on the arch along the Shinarump Unconformity. Later movement of the structure during the Late Cretaceous Sevier orogeny (Gow,

1950; Ritzma, 1955; Kopper, 1962; Tweto, 1975; Gries, 1983; Pang and Nummedal, 1995) may have created a foreland-basin high at the floor of the Western Interior Seaway. This topographic feature may have influenced Late Cretaceous sedimentation and facies architecture, including that of the Prairie Canyon Member of the Mancos Shale (Cole and Young, 1991).

Further structural development of the Douglas Creek Arch occurred during the Laramide orogeny and created its modern morphology. During that time, the Uinta and Piceance Creek Basins began to subside, and the Douglas Creek Arch may have acted as a hingeline between the two subsiding basins (Johnson and Finn, 1986).

3. Uinta and Piceance Creek Basins

The Uinta and Piceance Creek Basins flank the Douglas Creek Arch on the west and east, respectively. Both are structural and sedimentary basins that contain thick sequences of Paleozoic, Mesozoic and Cenozoic strata, all of which are hydrocarbon reservoirs in the subsurface (Sanborn, 1977). The basins began to subside during the Laramide orogeny and so are contemporaneous with the uplift of the Uncompahgre Plateau, Uinta Mountains, and the Douglas Creek Arch. These three positive topographic features contributed a significant amount of sediment to both of the basins in the Upper Cretaceous and Tertiary periods. Johnson and Finn (1986) have suggested that the Douglas Creek Arch served as a hingeline between the two subsiding basins during that period.

Economic quantities of oil and gas have been produced at a variety of stratigraphic levels in both basins. However, due to the great drilling depth (<15,000 feet), much of the oldest strata have not been brought into production. The Pennsylvanian-Permian Weber Sandstone is the oldest unit of economic significance. By 1977, it had produced 555 million barrels of oil at Rangely Field, Colorado. Wilson Creek Field, in the Piceance Creek Basin, Colorado, has produced 24 million barrels of oil from the Jurassic Entrada Sandstone and over 54 million barrels from the Jurassic Salt Wash Member of the Morrison Formation. There are enormous reserves of natural gas in the Cretaceous strata, but much of the Cretaceous section suffers from low permeability caused by clay infilling and/or cementation. The continual advance of gas production technology may one day make these reserves more accessible. Paleocene and Eocene strata of the Wasatch and Green River Formations are some of the most petroliferous deposits in the world, containing great quantities of gas, liquid petroleum, solid petroleum, oil shale, and bituminous sand. By the end of 1976, the Green River sediments had yielded over 117 million barrels of oil and 360 billion cubic feet (BCF) of natural gas, and more than 82 billion barrels of oil and 247 BCF of gas had been produced from the Wasatch Formation (Sanborn, 1977). One of the most exciting prospects for production of oil from these Tertiary rocks is the potential for extraction of economic quantities of oil from the oil shales of the Green River package. Donnell (1957) estimated oil reserves on the order of several hundreds of billions of barrels may exist within the Green River oil shales in the Piceance Creek basin alone.

References Cited (Appendix 1 only)

- Cole, R.D. and Young, R.G., 1991, Facies characterization and architecture of a muddy shelf-sandstone complex: "Mancos B" interval of Upper Cretaceous Mancos Shale, Northwest Colorado-Northeast Utah, *in* Miall, A.D., and Tyler, Noel, eds., The three-dimensional facies architecture of terrigenous clastic sediments and its implications for hydrocarbon discovery and recovery: Society of Economic Paleontologists and Mineralogists, Concepts in Sedimentology and Paleontology, v. 3, p. 277-287.
- Donnell, J.R., 1957, Preliminary report on oil-shale resources of Piceance Creek Basin, northwestern Colorado, U.S. Geol. Survey Bull. 1042-H.
- Gow, K., 1950, Douglas Creek gas field, *in* Guidebook to the Geology of Utah, No. 5: Utah Geological and Mineralogical Survey, p. 139-146.
- Gries, R., 1983, North-south compression of Rocky Mountain foreland structures, *in* Lowell, J.D., and Gries, R., eds., Rocky Mountain Foreland Basins and Uplifts: Rocky Mountain Association of Geologists, p. 9-32.
- Heyman, O.G., Huntoon, P.W., and White-Heyman, M.A., 1986, Laramide deformation of the Uncompahgre Plateau- geometry and mechanisms, *in* D.S. Stone, ed., New interpretations of northwest Colorado geology: Rocky Mountain Association of Geologists, p. 65-76.
- Johnson, R.C. and Finn, T.M., 1986, Cretaceous through Holocene history of the Douglas Creek Arch, Colorado and Utah, *in* D.S. Stone, ed., New interpretations of northwest Colorado geology: Rocky Mountain Association of Geologists, p. 77-95.
- Kopper, P.K., 1962, Douglas Creek anticline and adjoining area, *in* Amuedo, C.L., and Mott, M.R., eds., Exploration for Oil and Gas in Northwestern Colorado: Rocky Mountain Association of Geologists, p. 108-110.
- Pang, M. and Nummedal, D., 1995, Flexural subsidence and basement tectonics of the Cretaceous Western Interior Basin, United States: *Geology*, v. 23, p. 173-176.
- Ritzma, H.R., 1955, Early Cenozoic history of the Sand Wash Basin, northwest Colorado, *in* Ritzma, H.R., and Oriel, S.S., eds., Guidebook to the Geology of Northwest Colorado: Intermountain Association of Petroleum Geologists and Rocky Mountain Association of Geologists, p.36-40.

Sanborn, A.F., Possible future petroleum of Uinta and Piceance Basins and vicinity, northeast Utah and northwest Colorado, *in* Veal, H.K., ed., Exploration Frontiers of the Central and Southern Rockies: Rocky Mountain Association of Geologists, p. 151-166.

Stone, D.S., 1977, Tectonic history of the Uncompahgre Uplift, *in* Veal, H.K., ed., Exploration Frontiers of the Central and Southern Rockies: Rocky Mountain Association of Geologists, p. 23-30.

Tweto, O., 1975, Laramide (Late Cretaceous-Early Tertiary) orogeny in the southern Rocky Mountains, *in* Curtis, B.F., ed., Cenozoic History of the Southern Rocky Mountains: Geological Society of America Memoir 144, p. 1-44.

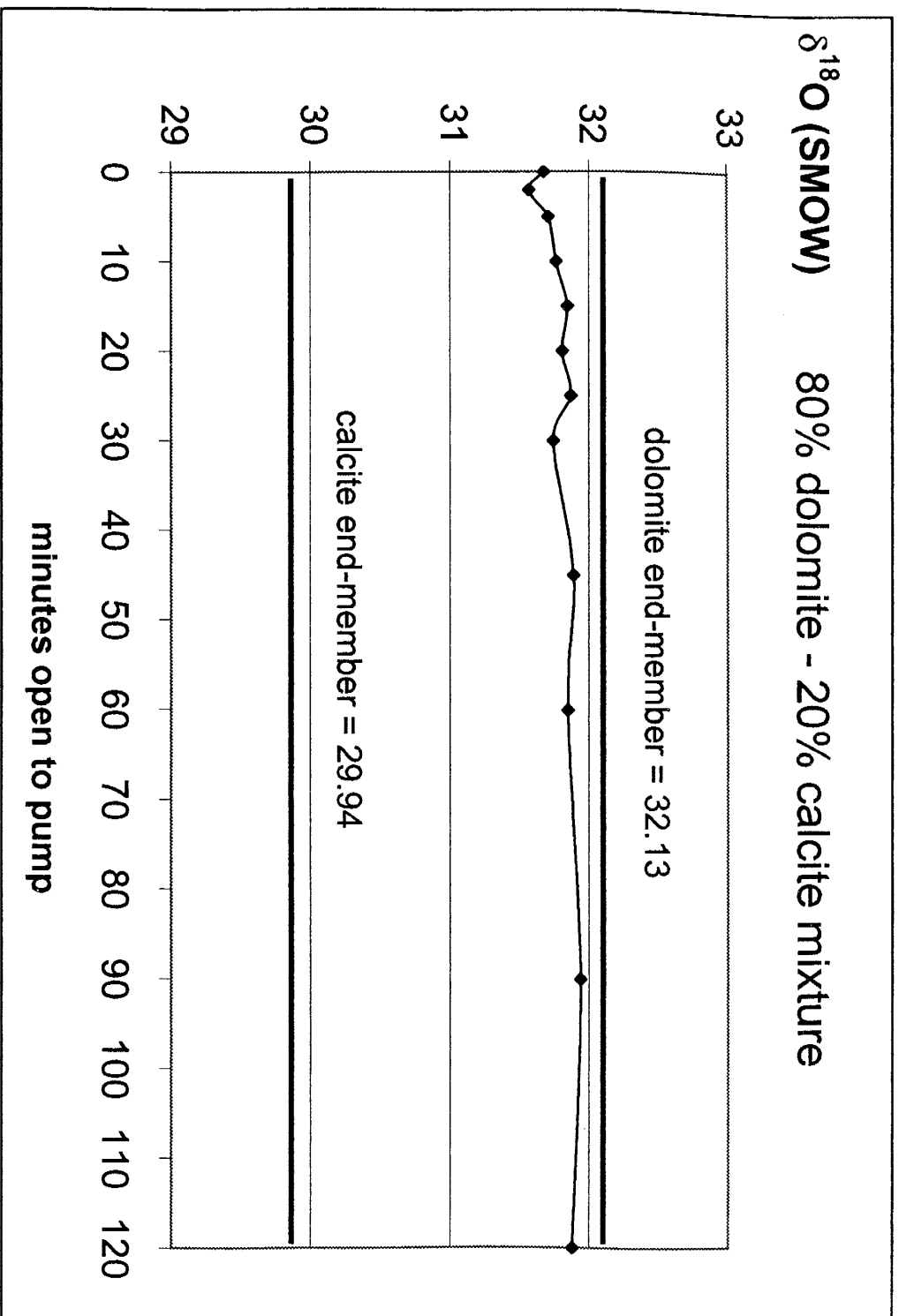
APPENDIX 2: CO₂ extraction for dolomite-calcite mixtures

A series of samples with a 80:20 ratio of dolomite:calcite (by weight) were prepared. Samples were tipped to allow the phosphoric acid reaction to begin and were left open to the pump for different lengths of time ranging from zero to 120 minutes to dissolve the calcite. The remaining dolomite was reacted overnight and extracted as described in Phillips et al. (1992; see also "Methods" section, above). The sample that was left open to the pump for 90 minutes most closely approached the end-member dolomite isotopic values (see attached table and figures).

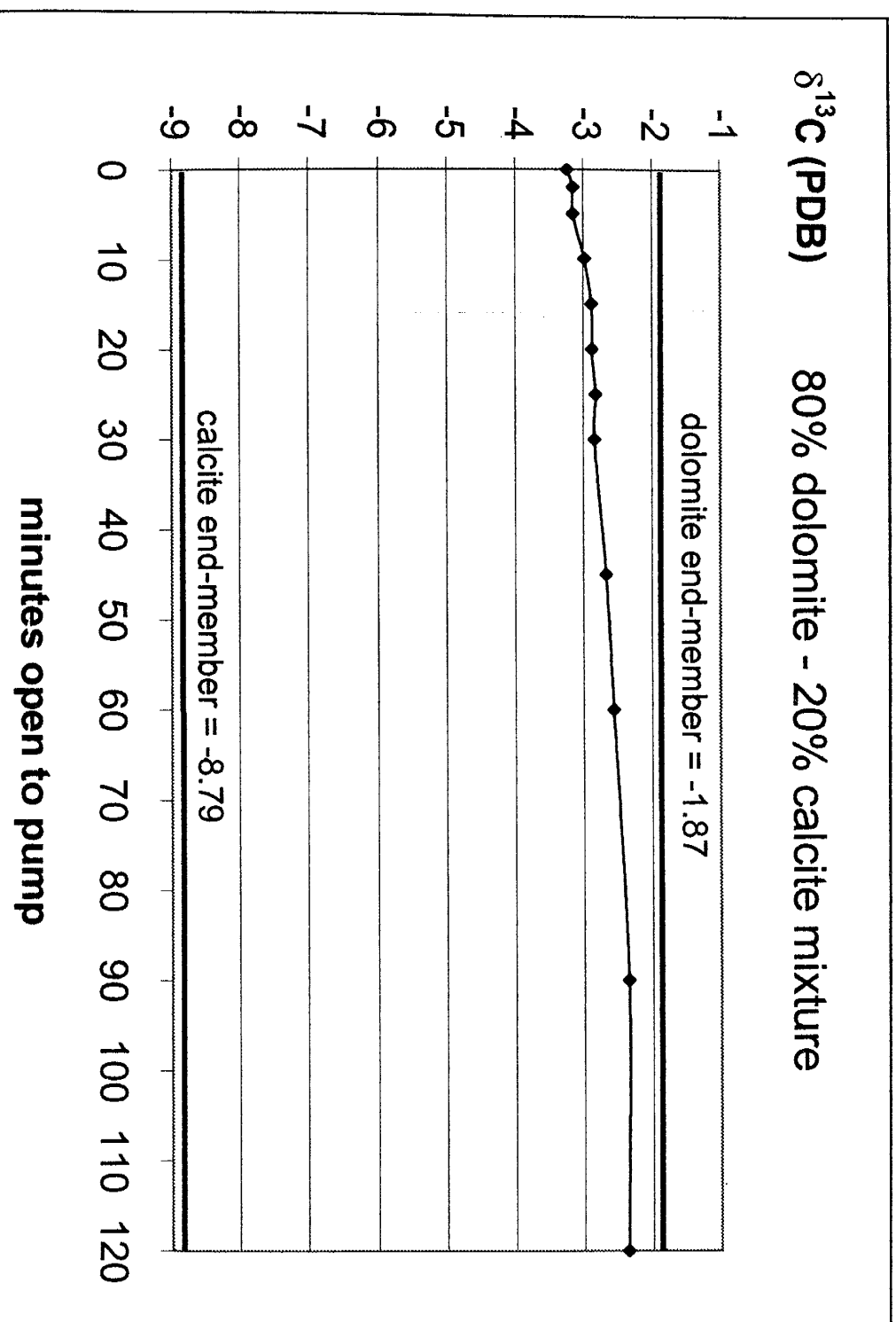
minutes pumped	$\delta^{13}\text{C}$ (PDB)	$\delta^{18}\text{O}$ (SMOW)
0	-3.239	31.67
2	-3.157	31.564
5	-3.152	31.703
10	-2.988	31.761
15	-2.89	31.843
20	-2.88	31.807
25	-2.828	31.867
30	-2.846	31.739
45	-2.681	31.886
60	-2.566	31.848
90	-2.359	31.938
120	-2.369	31.877
end-members		
100% calcite	-8.791	29.947
100% dolomite	-1.867	32.133

^{18}O (SMOW)

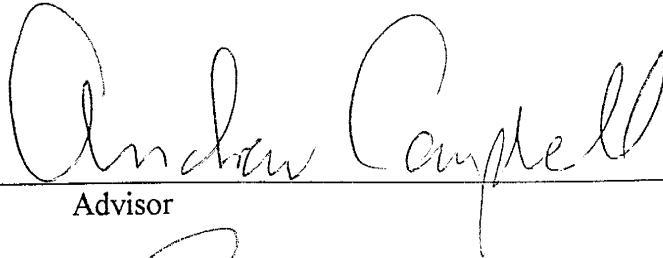
80% dolomite - 20% calcite mixture



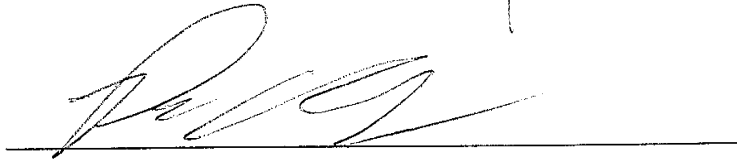
$\delta^{13}\text{C}$ (PDB) 80% dolomite - 20% calcite mixture

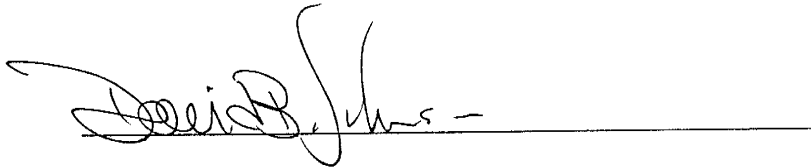


This thesis is accepted on behalf of the faculty
of the institute by the following committee:



Advisor





April 24, 1997

Date